MINERAL PROSPECTIVITY MAPPING USING INTEGRATED REMOTE SENSING AND GIS IN KERKASHA - SOUTHWEST ERITREA

Finhas Tsehaye Zerai

A Thesis

Submitted to the Graduate College of Bowling Green
State University in partial fulfillment of
the requirements for the degree of

MASTER OF SCIENCE

August 2023

Committee:

Peter Gorseveski, Committee Chair

John Farver

Kurt Panter

ABSTRACT

Peter Gorsevski, Committee Chair

This study evaluates the potential for mineral prospectivity mapping (MPM) within the Kerkesha area, southwestern Eritrea using remote sensing and geochemical data analysis. The Advanced Spaceborne Thermal Emission and Reflection Radiometer (ASTER) remote sensing data was used for mapping zones of hydrothermal alteration, while assessment of geologic structures is based on automated extraction of lineaments from a digital elevation model. Integration of these alteration and structural dataset with surface geochemical data were used in identifying pathfinder elements associated with Au-Cu-Zn mineralization as well as evaluating and delineating anomalous mineralization regions in this relatively underexplored region of Arabia Nubia Shield (ANS). Specifically, the modeling approach for the extraction and the interpretation of mineralization-related spectral footprints uses selective principal component analysis (SPCA), while the lineament features, which were extracted from different digital terrain models, were integrated with the soil geochemical data and modeled by principal component analysis (PCA). The results reveal a northeast-southwest trend of lineaments, delineate zones of hydrothermal alteration which indicate presence of multi-deposit type mineralization, and identify pathfinder elements. In addition, Au-Cu-Zn anomalous zones are extracted by one class support vector machine (OCSVM) and performances of such classification is validated by Kruskal-Wallis and Pearson's Chi-square tests. The results show significance in differences between the anomalous and non-anomalous zones and existence of a relationship between known mineral deposits and predicted anomalies. The proposed MPM shows promising results for robust automated delineation and understanding of mineralization processes.

Dedicated to my parents Mr. Tsehaye Zerai and Mrs. Tadelesh Ghebretinsae

ACKNOWLEDGMENTS

It has been a great learning experience working under supervision of Dr. Peter Gorseveski, my advisor, in accomplishing this research. I thank you greatly for your tireless dedication, patience and efforts at all stages of the work; most importantly, for showing me the way into the realm of spatial data analysis and for the unreserved sharing of your knowledge. Dr Kurt Panter and John Farver, your comments and questions helped me address important components in the mineral prospectivity endeavors, for which I am indebted.

Alasdair Smith – technical director of Alpha exploration, here is my turn to formally thank you for your positive influence in my professional development; more particularly for allowing me the access to the immense geological data of the study area on which the thesis work was anchored. I am also grateful to Mr. Tewelde Haile and Dr. Michael Gazley for delivery of a refined data. Moreover, the advice from Dr. Shawn Hood and Dr. Michael Gazley was a cornerstone that helped me orient the thesis direction, for which I remain grateful.

Without all-rounded support from my parents and siblings as well as close family members and friends, I would not have accomplished this task, hence a deservedly highest appreciations are accorded to you. Special thanks to my siblings Saron and Abel are befitting, for your unwavering support in my arduous journey that saw me travel several times between six countries, in just less than two years, to be at this milestone. To my friends, in those countries, who hosted me during the journey, I also express my gratitude.

Further, I seize this opportunity to extend my appreciation to all SEES faculty members for your support and empathy; particularly Prof. Kefa Otiso, graduate coordinator, for facilitating additional scholarship award that helped complete the thesis. Last, I would be remiss in my duty if I do not acknowledge my BGSU-GA colleagues for being there when needed.

TABLE OF CONTENTS

INTRODUCTION

The field of mineral exploration is often challenging given the complexity of mineralization processes and dynamics of several geological processes. Presently the challenge is even more pronounced as many deposits have already been discovered, but the advent in exploration technologies in the wake of availability of multi-source spatio-temporal datasets and new data mining approaches play paramount role for identifying new potential zones. Among such advancements are the use of remote sensing (RS) technologies which have proved their importance in the exploration campaign, particularly when they are integrated with geochemical and structural analysis (Harris et al., 1998; Rajendran and Nasir, 2017; Tangestani et al., 2005; Tayebi et al., 2014). The importance of such technologies is more enhanced by availability of open-access datasets from sensors such as the US/Japan Advanced Spaceborne Thermal Emission and Reflection Radiometer (ASTER) and spatial analytics performed by geographic information systems (GIS), machine learning (ML), and traditional statistical methods such as the principal component analysis (PCA).

For instance, the wealth of multi-source datasets allows for synergetic fusion of data and mapping of surficial minerals. In this respect GIS provides a framework for integrating and combining various datasets for mineral prospectivity mapping (MPM), while geovisualization methods provide an interactive mapping, exploration, and visualization tool that can identify different spatial patterns or anomalies. Such synergy is further bolstered by the advent of ML techniques that are gaining more attention in MPM as well as identifying pathfinder elements and geochemical anomaly by integrating and, concurrently, reducing multivariate dimensions of datasets (Carranza, 2011; Carranza and Laborte, 2015; Chen and Lin, 2014; Gazley et al., 2021; Grunsky and Caritat, 2020; Hood et al., 2019; Rodriguez-Galiano et al., 2015; Sadeghi et al., 2015; Xiong and Zuo, 2016; Zekri et al., 2019; Zhang et al., 2019; Zuo et al., 2019). The importance of pathfinder elements in mineral exploration is well known in the discovery of deposits in different depositional environments, in which an easily found element infers location of target elements and ores that are often complex to find (Balaram and Sawant, 2022; Gale, 2003; Hale, 1981; Kadel-Harder et al., 2021; Nude et al., 2012).

Over the past two decades, the main application of RS technology in MPM has been focused on the detection of hydrothermal alteration using visible and near infrared (VNIR) and short wavelength infrared (SWIR) regions of the electromagnetic spectrum (Harris et al.,1998). As such, ASTER data have been widely used in lithological mapping and mineral exploration because of its ability for acquiring absorption features located in SWIR that are representative for many rock-forming and alteration minerals (Abrams and Hook, 1995; Pour and Hashim, 2012). Moreover, ASTER's VNIR and thermal infrared (TIR) data provide sufficient capability for identification of vegetation and iron oxide minerals in surface soil. Additional capabilities in the detection of carbonate and silicate minerals is enabled by the low reflectivity in the ASTER's VNIR-SWIR and the high emissivity in the TIR spectral bands (Bedell, 2001; Ninomiya, 2003; Rockwell and Hofstra, 2008).

The relationship between various hydrothermal alterations, mineral deposits and geological structures is strongly established by ore forming processes where hydrothermal fluids react with mineral constituents in the host lithologies as they move through structures or lithologically controlled pathways (Chisambi et al., 2021; El-Desoky et al., 2021; Lowell and Guilbert, 1970a). As a result, several linked alterations such as propylitic, phyllic, argillic, advanced argillic and silicification occur with gold-copper (Au-Cu), silver (Ag), and/or lead-zinc (Pb-Zn) mineralization (Noori et al., 2019). Based on the widely used model developed by

Lowell and Guilbert (1970a) porphyry copper deposits (PCD) are typically characterized by potassic, phyllic, advanced argillic, argillic and propylitic alteration zones from center towards the outward margin of mineralized igneous body (Mavrogonatos et al., 2018; Salehi and Tangestani, 2018). Surficial manifestation of PCD deposits as well as other deposits such as high sulfide Au-Cu, Au and base metal sulphides, and copper-nickel (Cu-Ni) deposits in the lateritic terrain is a gossan veneer. This surficial cover is formed as a result of oxidation of iron-bearing minerals exposed on the Earth's surface and/or associated with hydrothermally altered rocks, which makes mapping of iron oxide-hydroxide minerals of prime importance in mineral prospecting (Rockwell, 2004; Sillitoe, 2010; Swayze et al., 2000). Furthermore, records of silicic alteration associated with gold bearing volcanogenic massive sulphide (VMS), orogenic gold, epithermal Au and high sulfidation epithermal Cu-Au deposits exist (Aliyari et al., 2007; Chang et al., 2011; Dubé et al., 2007; Sander and Einaudi, 1990). Respectively, targeting and prospecting through analysis of ASTER for those alterations and minerals becomes versatile and feasible primary step in mineral exploration regime.

The present study offers an integrated approach that combines RS, GIS and ML in predictive MPM of Kerkasha, southwestern Eritrea (Figure 1). This novel approach embeds spectral and structural information into geochemical dataset which are, singularly and/or collectively, analyzed with an aim to: *a)* explore and delineate hydrothermal alteration zones *b)* highlight mineralizing environment; *c)* predict mineralized zones and determine pathfinder element assemblage of mineralization; and *d)* predict anomalous zones of mineralization.

BACKGROUND

Approaches for MPM

Different image processing techniques for mapping hydrothermal alteration zones using ASTER data exist, including matched-filtering (Harsanyi and Chang, 1994), PCA (Crosta et al., 2003; Tangestani et al., 2005), spectral angle mapper (SAM) (Galvão et al., 2005; Kruse et al., 1993; Noori et al., 2019; Tangestani et al., 2005) and band ratios (Crowley et al., 1989; Perry and Vincent, 2009). Other commonly-used approaches include decorrelation stretching, linear spectral unmixing and mixture tuned matched filtering (Rajendran and Nasir, 2017). Integrative methods that combine different techniques such as PCA and SAM (Honarmand et al., 2012) are also used for identification of such alteration zones. Although PCA-based MPM is the most popular technique for dimensionality reduction and processing RS datasets, the major drawback of this technique is that color composites are often difficult to interpret while the information of interest could be lost especially from unused components (Kwarteng and Chavez, 1989a). However, the selective principle component analysis (SPCA) method, which assumes that only a subset of the image bands contain useful information for a specific application, increases the chances for defining unique principal components (PCs) which have representative spectral features of specific mineral or mineral classes (Crosta et al., 2003; El-Desoky et al., 2021; Loughlin, 1991; Noori et al., 2019, 2019; Ruiz-Armenta and Prol-Ledesma, 1998; Tangestani et al., 2005).

In the past several decades, many frequency-based statistical methods have been employed to identify geochemical anomalies (Chen and Lin, 2014; Chen and Wu, 2017; Grunsky and Caritat, 2020; Zuo et al., 2016). Some of the classical methods include *k* standard deviations above and below arithmetic mean (Hawkes and Webb, 1963), univariate analysis (Govett et al., 1975), probability graphs and multivariate analysis (Sinclair, 1974). These methods, however, fail to consider the complex and nonlinear patterns from high-dimensional variables (Afzal et al., 2016; Xiong and Zuo, 2016; Yousefi et al., 2014; Zuo et al., 2019). Such complexity and nonlinear relationship are considered by ML algorithms, using: *a)* supervised classification algorithms such as random forest (RF), support vector machine (SVM) and artificial neural networks (ANN) (Carranza and Laborte, 2015; Rodriguez-Galiano et al., 2015); and *b)* unsupervised algorithms such as clustering (Templ et al., 2008), one-class support vector machine (OCSVM) (Chen and Wu, 2017), continuous restricted Boltzmann machines (Chen et al., 2014), and isolation forest (Chen and Wu, 2019) .

That said, MPM and geochemical anomaly signatures are often hindered by irrelevant and/or redundant variables in a geochemical dataset. Therefore, it is necessary to extract significant features by means of dimensional reduction, from which pathfinder elements are identified, before applying unsupervised ML algorithms for anomaly detection. As a remedy for this, PCA, hierarchical clustering (HC), stacked denoising autoencoder (SDAE), or deep belief network analysis are first applied to the multivariate datasets (Carranza, 2011; Sadeghi et al., 2015; Wang et al., 2020; Xiong and Zuo, 2020; Zekri et al., 2019). In this perspective, recent works in geochemical anomaly detection have focused on hybrid models where multivariate datasets are first involved in a training analysis to learn the representative features of the geochemical data for non-linear dimensionality reduction. The features learned from the original data are then used to automatically train and test several models by ML classifiers in the detection of geochemical anomalies (Wang et al., 2020; Xiong and Zuo, 2020).

Recent application of predictive ML approach in the study area focused on improving historic bedrock maps in sites with transported overburden. Digital terrain model, ASTER , pre-existing geological maps and geophysical data (magnetic and radiometric) were used for the supervised RF bedrock mapping, in which the RF classification was assisted by PCA (Hood et al., 2019). The derived bedrock maps were further integrated with machine-learnt regolith maps that were generated by combining ASTER spectral data and radiometric data using self-organizing maps (SOM) approach. The products enabled *z*-score normalization of regional soil geochemical data of the study area using regolith type and bedrock geology in an attempt to remove their bias from the soil geochemistry. These accentuated the signal that reflects metasomatic processes and elemental anomalism related to mineralization (Gazley et al., 2021).

Regional Geology

Geologically, Eritrea is characterized by Arabian Nubian Shield (ANS) Precambrian basement. The ANS is composed of granitoid-greenstone belt terranes and mid-crustal gneissic terranes that underlie parts of Egypt, Sudan, Eritrea, Ethiopia, Israel, Jordan, Saudi Arabia, and Yemen, on either side of the Red Sea (Barrie et al., 2007), and it is unconformably overlain by Mesozoic to Cenozoic rock (Andersson et al., 2006; Barrie et al., 2007; Drury and Berhe, 1993; Johnson et al., 2011; Stern, 1994; Teklay, 1997).

The regional geology is divided into four distinct terranes on the basis of distinct stratigraphic and structural characteristics: the Barka terrane to the far west (predominantly amphibolite-grade metasedimentary and mafic gneisses), the Hagar terrane to the north (principally mafic metavolcanic rocks, including ophiolite-like assemblages), the Nakfa terrane, the largest of the four (granitoid greenstone belts and syn- to post-tectonic granitoid rocks), and the Arag terrane to the east (granitoid and metasedimentary rocks) (Andersson et al., 2006; Berhe, 1990; Drury and De Souza Filho, 1998; Teklay, 1997). Each terrane is structurally bound by north-south trending shear zones. The late Neoproterozoic collision between East and West Gondwana concentrated transpression in the juvenile crust of the Arabian Nubian Shield along at least two steep, curvilinear crustal-scale belts: the Augaro-Adobha Belt (AAB), which hosts the western half of the study area, and the Asmara-Nakfa Belt (ANB) to the east (Figure 1a) (Fritz et al., 2013; Ghebreab et al., 2009; Johnson et al., 2011; Woldehaimanot, 2000).

In terms of mineralization, ANS is well known for orogenic gold, VMS Cu-Pb-Zn-Au, PCD and rare metal deposits (Barrie et al., 2016; Johnson et al., 2017) as well as epithermal Au, reduced intrusion-related Au, carbonate-replacement base metal and iron oxide-Cu-Au (Abd El Monsef et al., 2018; Bierlein et al., 2020, 2016; Perelló et al., 2020). In Eritrea's ANS the mineralization is dominated by the two north-trending curvilinear greenstone belts that formed during the transpressional deformation, AAB & ANB (Figure 1a). The Au and base metal mineralization in the AAB includes the Augaro district where Zara and Bisha world-class deposits are located, while ANB includes the Asmara districts (e.g. Emba Derho, Adi Nifas and Gupo VMS deposits) that are associated with various locations of gold deposits (Barrie et al., 2007; Gazley et al., 2021; Ghebreab et al., 2009; Johnson et al., 2017).

Geology of the Study Area

As presented in Figure 2 several outcrops and overburdens are identified in the study area. Out of these three main volcano-sedimentary units and granites were identified, namely: *a)* basalt dominated unit of mainly mafic volcanics and subordinate volcaniclastics with presence of some andesitic units with prominent gabbro and dolerite intrusions; *b)* andesitic unit with extensive volcaniclastics, as well as distal sediments and sporadic gabbro sills; *c)* felsic volcanic and volcaniclastics, some of which are banded with basaltic units which may be evidence of bimodal volcanism; and *d)* syn- to late-tectonic granitic intrusion (Alpha exploration, 2023). Stretching in northeast-southwest intermediate metavolcanics and metavolcaniclastics also exist, while felsic shists and metavolcanics extend in north-northeast and south-southwest.

Chlorite, epidote, and carbonate alteration of the above rocks is typical throughout the study area. Thani-Ashanti (2013), as cited in Gazley et al. (2021), attributed this alteration to a ubiquitous regional metamorphic event; silicification, hematite and sulphidation type of alterations also exist in Kerkesha. The petrology of the granitoid samples in the northern part of the study area are consistent with regional greenschist facies metamorphism by the chloritisation of amphibole and biotite. This regional foliation has a 30^{o} - 50^{o} trend with lithological contacts offset by nothheast-trending shear zones, and the layer parallel structures are offset by north-trending faults that may have a sinistral component (Gazley et al., 2019).

Ferruginous quartzites, gossans and cherts are prevalent, and these zones cover the northeastern extent of a gold mineralized belt which includes historic mines found in the southwestern region. Gold mineralization associated with silica, carbonate and sericite alteration, galena and chalcopyrite, and malachite-rich gossan occurrences also exist. Further, Au-Cu-Ag mineralization from surface and drilling rock chips has been reported. Hence the area is considered prospective for VMS (Au-Cu-Zn) and orogenic Au deposits as well as Cu-Au porphyry system at depth (Alpha exploration, 2023).

DATASETS AND PREPROCESSING

ASTER and Digital Elevation Data

ASTER satellite images, digital elevation model (DEM) and surface soil sample geochemistry were the main datasets used for the MPM. The imagery from the ASTER optical and thermal sensors aboard an operational TERRA satellite, which is the flagship of the Earth Observing System (EOS), were downloaded in Geographic Tagged Image File Format (GeoTIFF) format from the Japan's Ministry of Economy, Trade and Industry (METI) database (https://gbank.gsj.jp/madas/map/). The utilized imageries are Level-1A products which contain unprocessed digital numbers for each band at full resolution with coefficients for conversion to at-sensor radiance, and geometric correction are supplied in the metadata. The ASTER scenes are composed of 14 spectral bands organized in separate instrument subsystems where 3 bands are in the VNIR with 15-meter spatial resolution, 6 bands are in SWIR with 30-meter spatial resolution and 5 bands are in TIR with 90-meter spatial resolution. The swath width for all sensor subsystems is 60 km while the temporal resolution of the sensors is 16 days (Abrams, 1999, 2000). Detailed attributes of the bands are shown in Table 1. The DEM data was also downloaded from METI's database of ASTER global DEM version 3 in GeoTIFF format with 30-meter posting intervals (https://gdemdl.aster.jspacesystems.or.jp/index_en.html).

ASTER SWIR data acquired after April 2008 are not usable because the scenes show saturation of values and contain severe striping caused by anomalously high SWIR detector temperatures (Sekertekin and Arslan, 2019; NASA / JPL, 2009). In this study, scenes were acquired prior to the malfunctioning date when all ASTER sensors (VNIR, SWIR and TIR) were active. Considering the data availability and quality (i.e., cloud free), a total of three spatially overlapping scenes acquired on 01/21/2007 and 01/14/2007 were selected where two images were acquired on the same date.

First, the obtained georeferenced scenes were projected to the UTM Zone 37 North using WGS-84 datum, before digital numbers (DNs) were converted to at-sensor radiance. The conversion from radiance to top of atmosphere (TOA) reflectance for the VNIR and SWIR bands used dark-object subtraction (DOS) method. For the TIR bands the at-sensor radiance was converted to brightness temperature which in turn was converted to land surface temperature (LST). The relationship between the normalized difference vegetation index (NDVI) and the emissivity of terrestrial materials that often lies between 0.7 and 1.0 was used to estimate the land surface emissivity (LSE). The computed LSE was then used for the correction of brightness temperatures and to estimate the LST by inversion of the Planck function. The temperatures were calculated in Celsius degrees (Diaz et al., 2021; Ndossi and Avdan, 2016).

Geochemical Data

The geochemical assay data that was provided by Alpha Exploration LTD, contained approximately 11,000 systematically collected soil samples covering the study area (Gazley et al., 2021). The sampling density was ~ 500 x 500 m and ~ 100 x100 m at regional and prospect scale, respectively. A total of 36 % of the samples are part of the regional sampling while the rest of the samples are part of prospect scale sampling (Figure 1b). In both sampling campaigns, 2 - 3 kg samples of soil were collected from shallow holes (5 - 25 cm deep). The air-dried samples were sieved to < 180 μm in order to provide homogenized material (Cardoso Fonseca and Martin, 1986). Approximately 2 kg was stored in-house, while a 60-g scoop sample was sent to ALS Geochemistry laboratory (Loughrea, Ireland) for Au analysis, and 150 g was sent to local

Olympus workstation for portable X-ray florescence (pXRF) multielement analysis and sample archiving (Gazley et al., 2021).

Those samples weighing 150 g were analyzed on an Olympus Vanta VMR, 8-50KV, Rh X-ray tube, pXRF instrument while handling and procedures were consistent with industry best-practices (Gazley et al., 2021). The Olympus workstation was used to process the samples in 40 mm sample cups covered by 4 µm prolene film with 20s per beam analysis time in Geochem mode using data correction and handling techniques consistent with industry best-practice that included normalization of data to a selected standard reference material (SRM) and matrix matching (Fisher et al., 2014; Gazley et al., 2021; Gazley and Fisher, 2014). As per customary analytical steps several standard samples were included and their analysis were performed using the pXRF to calculate correction factors for the analysis of the other samples. This resulted in a dataset that is considered robust and reliable for a total of 28 elements: Mg, Al, Si, P, S, K, Ca, Ti, V, Cr, Mn, Fe, Ni, Cu, Zn, As, Rb, Sr, Y, Zr, Nb, Mo, Ag, Sn, W, Pb, Th and U (Gazley et al., 2021). Pulp packets that contained the 60 g scoop samples were sent to ALS for trace level Au analysis where 25 g of the scoops were treated by aqua regia extraction (method Au-TL43) followed by ICP-MS analysis, proving a detection limit of 0.001–1 ppm. Such an amount allowed for a duplicate analysis or repeat of the sample in the event of an accident or laboratory repeat (Gazley et al., 2021).

Due to missing and censored values (less than the detection limit) in the observations, the original dataset was reduced to a total of 22 elements for the analysis consistent with the recommendation of Martín-Fernández et al. (2012). The elements in the final dataset were Mg, Al, Si, P, S, K, Ca, Ti, V, Cr, Mn, Fe, Ni, Cu, Zn, As, Rb, Sr, Y, Zr, Nb and Pb. The final dataset contained elements with > 70 % of them having non-missing values, while the missing values for these elements (and laboratory Au analyses) were replaced by imputation function for compositional data using *k*-nearest neighbor method in R. This imputation assigns a value to a missing compositional data by inference from the value of the products or processes to which it contributes (Gazley et al., 2021; Hron et al., 2010; Templ et al., 2011). These resulted into dataset with values for a total of 23 elements of each of the samples. Such imputation of values, and the subsequent analysis of the dataset using standard techniques for complete data, are explained in detail by Gazley et al.(2021) and Hron et al.(2010).

Transformation of Geochemical Data

Soil geochemical data is a compositional data which consists of sub-compositions or vectors whose components are the proportions or percentages of the whole composition which equals 100 % or 1.0 (i.e., chemical composition of a rock expressed as parts per million (ppm) or weight percent (wt %)). However, proportions are constrained to a constant sum and restricted to the positive number space while variables are not free to vary independently (i.e., increase in the value of a data point requires the other data points to decrease) which yields non-independence of data points and limits the use of parametric statistical techniques (Carranza, 2011; Filzmoser et al., 2009; Grunsky and Caritat, 2020). To avoid incorrect inferences and limitations for analyzing raw compositional data the use of transformations using the logarithms of the ratios between the components is often required (Aitchison, 1986). The central log transformation (clr) that was used here is a commonly used transformation method that applies the log of the ratio between observed frequencies and their geometric mean (Carranza, 2011). For example, each component is standardized by dividing with the geometric mean of all components and resulting ratios are returned as logarithms.

METHODOLOGY

The methodology for the extraction of anomalous zones used in this study is illustrated in Figure 3. The figure first shows the integration and the preprocessing steps associated with the DEM, soil geochemistry and ASTER datasets that culminated into identification of pathfinder elements and generation of PCA predictive model of anomalous mineralization zones. In the process, the hydrothermal alteration zones generated by SPCA from ASTER were used for the model development while the zones outside of the hydrothermal alteration zones were used for the predictions. The predictive models were generated from the integrated dataset that contained the soil geochemistry and the extracted lineament densities. A total of five predictive models that are representative of the alteration zones and iron oxide - hydroxide minerals were generated and subsequently subjected to OCSVM classification using different thresholding values. Finally, the classified predictions were spatially aggregated by minority and majority rules. The validation in this approach was tested by Kruskal-Wallis (K-W) and Pearson's Chi-square tests (χ^2).

Image Processing by Principal Component Analysis (PCA)

PCA transformation is a dimensionality-reduction method that decreases spectral redundancy in multiband datasets by creating new auxiliary bands (PCs) which are uncorrelated linear combination (eigenvector loadings) of the original bands (Masoumi et al., 2017; Noori et al., 2019; Sheikhrahimi et al., 2019). For example, the new PCs contain the unique contribution of eigenvector loadings for absorption and reflection bands of alteration mineral or mineral groups and they are used for elucidating different underlying geological processes (El-Desoky et al., 2021; Grunsky, 2010; Safari et al., 2018; Sheikhrahimi et al., 2019). Usually, the first PC is associated with the largest explained variance while variances in each subsequent PC diminishes.

Such variances are related to spectral responses of various surficial materials (i.e., minerals, rocks, soil) that are influenced by the statistical dimensionality of the data. For example the first PC can be associated with regional geological patterns (i.e., terrain characteristics or lithological settings) while the subsequent PCs can reveal subdued features like alteration or mineralization (Grunsky et al., 2014). In each PC, the positive loadings depict features as bright pixels (higher spectral purity) while negative loadings depict features as dark pixels (lower spectral purity) (Crosta et al., 2003; Crosta and Moore, 1989; Loughlin, 1991).

In this research, the preprocessed VNIR, SWIR and TIR bands from ASTER were used to map hydrothermal alteration zones by SPCA, a variant of PCA. This SPCA, also known as directed PCA (DPCA) or Crosta method was applied to selective bands that contained strong reflection or absorption features for a particular alteration (Figure 4) (Crosta et al., 2003; El-Desoky et al., 2021; Kwarteng and Chavez, 1989b; Noori et al., 2019; Tangestani et al., 2005). The spectral responses were identified from the known ASTER band indices for hydrothermal alteration mineral mapping and by relating to the spectral responses of main mineral assemblages for a given alteration zone (Abdelsalam et al., 2000; Honarmand et al., 2012; Mars and Rowan, 2006; Noori et al., 2019; Rowan and Mars, 2003). The endmember minerals that were used in this research included kaolinite, allunite, montmorillonite and dickite for argillic alteration; muscovite (sericite) and illite for phyllic alteration; epidote and chlorite for propylitic alteration; and quartz for silicic alteration (Honarmand et al., 2012; Mavrogonatos et al., 2018; Testa et al., 2018).

Accordingly, multiple triplets of bands from VNIR-SWIR region (0.4-2.5µm) (Table 2a,b,c, and d), namely bands 1,2,4, bands 4,5,6, bands 5,6,7 and bands 7,8,9 were selected to enhance zones of iron oxide - hydroxide minerals, argillic, phyllic, and propylitic alterations respectively. The TIR bands 12,13,14 (Table 2e) were also selected to map silicic alterations, based on the diagnostic spectral responses of silicic alteration and/or based on such spectral responses of quartz, which is the key endmember mineral for silicic alteration (Honarmand et al., 2012; Livo et al., 1993; Mojeddifar et al., 2013; Noori et al., 2019; Pearson et al., 2017). In performing the SPCA, the VNIR and TIR bands of the ASTER data were resampled by the cubic convolution (bicubic spline interpolation) resampling method for obtaining consistent spatial 30 m resolution.

Moreover, the threshold values for the selection of higher spectral purity associated with the PCs from the SPCA were enhanced by fuzzy sets. The fuzzy set approach presented by Zadeh (1965) allows for an explicit incorporation of uncertainty by characterization of the degree of membership that ranges between 0 (full-non-membership) and 1 (full membership). The fuzzification process that transforms a crisp set to a fuzzy set uses various fuzzy membership functions such as linear increasing, linear decreasing, triangular, sigmoidal, and *j*-shaped that can be developed by computing probability density or by expert knowledge (Burrough et al., 2015; Gorsevski et al., 2006). The approach here, implemented sigmoidal increasing and decreasing membership functions defined by 2 control points (a and b). The fuzzy functions and control points used for each alteration shown in Table 3 represent the 3rd and 97th percentiles. However, multiple threshold (cut-off) values were examined (i.e., 0.85, 0.90, 0.95 and 0.97) to fuzzify the PCs for elucidating minerals and zones of alterations that are likely linked with mineralization. The results reported here are based on a threshold of 0.95 membership value for all alteration zones.

Lineaments Mapping

Geological structures, such as faults, shear zones, lithological discontinuities and foliations act as conduits for mineralizing hydrothermal fluids, and when intertwined with alterations zones are ultimately considered as highly prospective; these structures are expressed by lineaments (Chisambi et al., 2021; El-Desoky et al., 2021). The lineaments in this research were extracted from DEM terrain derivatives including hillshade, slope and profile curvature. The features were interpreted as lines drawn in relation to linear or semi-linear terrain forms such as fault scarps, river valleys, ridgelines and other landforms. Prior to the extraction of the lineaments, the DEM was pre-processed for reduction of errors and noise by applying Sobel filtering (or smoothing) which consisted of a 5 x 5 kernel size. The lineaments from the hillshades which are associated with variations in sun illumination and changes in slope or aspect angles (i.e., changes in shadows) were illuminated from a total of eight different azimuth angles (0º, 45º, 90º, 135º, 180º, 225º, 270º, 315º). The extraction from the illuminated relief maps was based on a threshold value of 5 % from their cumulative frequency curves but other threshold values (i.e., 3%, 7 % and 10%) were also explored. The approach produced a total of eight binary maps of lineaments which were consequently aggregated into a single overlay map. The extraction of lineaments associated with the abrupt changes in slope gradient also used a threshold value of 5 % from the cumulative frequency curve. On the other hand, the profile curvature which is representative of concave and convex features such as river valleys (with negative values) and ridges (with positive values) required two different threshold values which are associated with the lowest and the highest percentiles (i.e., 5 % and 95 %). The post-processing procedures that were implemented to all binary terrain derivatives maps included methods such as thinning, vectorization and generalization as well as cleaning of small segments less than 50 m. Lastly, the three binary maps were combined into a single map which was used for producing directional statistics and for calculating density of lineaments.

Soil Geochemistry Analysis

PCA was applied to the transformed CLR geochemical data for determining multi-element assemblage(s) or pathfinder elements and zones of mineralization. The training sample for the PCA was extracted from the alteration zones generated by the SPCA, followed by alteration-specific PCA predictive model applied on the scaling-transformed dataset. Besides the compositional geochemical data, the lineament density values were also used as an additional variable in the analysis. For each alteration, a total of 10 important PCs were kept, which explained variances that ranged between 80 and 85 %. (Cattell, 1966; Jolliffe, 2011; Kaiser, 1960)

The loadings of PCs were interpreted according to their magnitude, sign and statistical significance. For instance, PCs containing high magnitude (positive or negative) loadings of target elements are considered as key components in determining polymetallic deposit existence and pathfinder elements related to the sought after deposits. In each of the alteration and iron oxide-hydroxide mineral setting, pathfinder elements were explored by studying their interrelationship with the high contributing loadings of the target elements by examining several combinations of PCs in bi-dimensional spaces (biplots); these PCs are mainly considered to manifest alterations, mineralization / mineral deposits and lithology (Sadeghi et al., 2015). Importantly, the spatial visualization of predicted scores of the individual PCs was achieved by implementing the inverse distance weighting (IDW) interpolation method. The interpolated maps were used to delineate zones with high positive or negative loadings, which in turn highlighted zones of mineralization and underlying lithologies (Grunsky, 1986; Sadeghi et al., 2015).

One-Class Support Vector Machine (OCSVM) Classifier

A variant of the classical SVM which is often used for anomaly detection through unsupervised classification is the non-parametric OCSVM classifier (Schölkopf et al., 2001). This OCSVM classifier was used in the study to separate the multivariate geochemical data into two-class binary solution of normal and anomalous cases. The algorithm maps the input data into a feature space with higher dimensions and iteratively finds a maximal margin hyperplane that can best separate the normal (non-anomalous) from the anomalous data samples. A detailed description of the algorithm can be found in Chen et al. (2017) and Wang et al.(2022).

The radial basis function (RBF) kernel is commonly used method to iteratively fit the non-linear boundary (the maximal margin hyperplane) that separates the anomalous from non-anomalous data samples. In addition, the *nu* (ν) parameter is used to specify desired fraction (upper bound) for two-class separation and *gamma* (γ) is the parameter of the RBF kernel method that governs the smoothness of the solution. The estimated output in a classified approach represents a discrete class where a value of 1 is taken as an anomaly and a value of 0 is taken as normal. In the presented work, the RBF kernel method was invariably kept the same, the gamma was set to 0.001, while *nu* was interchangeably set at 0.05, 0.20, 0.40, 0.60, and 0.80 for detecting classified anomalies into a total of 6 classes. For example, higher values of *nu* such as *nu* = 0.05 generates a total of 5 % of anomalies while the next lower level of *nu* = 0.20 generates a total of 20 % which contains the preceding 5 % and additional anomalies. Such an approach of repeated thresholding by different cut-off values can be useful for anomaly assessment and understanding of uncertainties in predicted anomaly maps.

Validation

The Kruskal-Wallis (K-W) test which is a non-parametric (distribution free) alternative to the one-way ANOVA, was used to compare the differences between the anomalous and non-anomalous groups of elements (Ostertagová et al., 2014). The null hypothesis of the K-W test is that the mean ranks of the groups are the same. In this research, the K-W was used to compare the mean ranks (medians) extracted from areas predicted as anomalous and non-anomalous for understanding discernment in spatial distributions of Au, Cu and Zn amounts.

The cross tabulations (or contingency tables) which describe the relationships between categorical (nominal or ordinal) variables along with χ^2 test was also used in the study. Specifically, the association between classes of predicted anomalies and existing location of mines (a total of 18 mines) was explored. The locational data of the mines was extracted by random sampling of 20 points per individual mine that were within 250 m buffer surrounding the mine.

The overall research involved several spatial analysis techniques; such analysis, along with the accompanying visualization tasks, were predominantly performed in R software environment, SAGA-GIS and QGIS software. Python environment's package "OneClassSVM" form the Scikit-learn (Sklearn) library for machine learning was also employed in performing the anomaly detection part of the analysis.

RESULTS AND DISCUSSION

Hydrothermal Alteration

The PCs generated by the SPCA from ASTER bands are shown in Table 2 where the eigenvector loadings of the PC images are representative of the spectral characteristics related to specific hydrothermal alteration minerals including *a)* argillic alteration; *b)* phyllic alteration; *c)* propylitic alteration; *d)* iron oxide-hydroxide minerals; and *e)* silicic alteration. In view of the spectral ranges of ASTER, the SPCA method for the argillic alteration used specific subset of bands that are representative of reflective feature (↑) in band 4 and absorptive response (↓) in bands 5 and 6 (Table 2a). By analyzing the eigenvector loadings from the three PC images of the SPCA transformation, it can be seen that PC3 contains the argillic mineral information. PC3 has the highest opposite signed loadings of band 4 (-0.5069) and band 5 (0.7288) as compared to the other two PCs. The dark pixels associated with the negative sign are normally expected to highlight this alteration type, however for visual consistency, the enhancements are opted to be portrayed as bright pixels. Hence by multiplying this PC with negative (or inverting the color), Figure 5a portrays an enhanced zone of argillic alteration in bright pixels. Subsequently, the threshold value which segregate the highly altered zones were computed by fuzzy membership function applied to the PC3 (i.e., higher than 95 % threshold value). The fuzzified scores (i.e., possibilities between 0 and 1) which are representative of uncertainties related to the threshold value were generated by the sigmoidal-decreasing fuzzy membership function and the control points (a =0.0105 and b = 0.0503) from Table 3. Lastly, the highly altered zones with high membership values were colorized by rainbow color scheme and draped over the gray scale PC3 image.

The phyllic alteration has a significant spectral response in the ASTER SWIR region especially in bands 5, 6 and 7 (Table 2b). This contrasting high-magnitude opposite sign of eigenvector values associated with PC2 show high negative loadings from both band 5 (-0.5769) and band 7 (-0.6659) on the reflective end as opposed to the high positive loadings of the absorptive band 6 (0.4729). The inverted bright pixels by negative multiplication are representative of this alteration, while the highly altered zones calculated by fuzzy membership function are overlaid and represented by colorized image (Figure 5b).

The propylitic alteration has a significant spectral response in the ASTER SWIR region where high reflectance is present in band 7 and stronger absorption features are in bands 8 and 9 (Table 2c). PC1 in Table 2c has the highest opposite loading for band 7 (-0.7546) and band 9 (0.5717), and its subsequent inversion accentuates propylitic alteration in colorized pixels that are draped over enhanced bright pixels (Figure 5c). Pixels of iron oxide-hydroxide minerals are characterized by lower reflectance in bands 1 and 2 and higher reflectances in band 4 in the VNIR-SWIR spectral region (Table 2d). The PC1 in Table 2d has the highest opposite signed loadings from band 2 (-0.48248) and band 4 (0.822697), and it enhances pixels of iron oxide-hydroxide minerals in bright pixels with colorized highest membership (Figure 5d). The silicic alterations are identified in the ASTER TIR region where the low emissivity characteristics are associated with band 12 and high emissivity characteristics are associated with bands 13 and 14 (Figure 3). PC3 in Table 2e has high negative loading in band 12 (-0.5627), and high positive loading in band 13 (0.6864). The highly altered zones (i.e., pixels with high possibility) are colorized and overlaid over the enhanced PC3 image where bright pixels are representative of the silicic alteration (Figure 5e).

Interestingly, there is noticeable similarity in the spatial pattern of highly altered argillic, propylitic, and iron oxide – hydroxide minerals zones that extend roughly in northeast-southwest direction (Figures 5a, 5c and 5d), and the locations of hydrothermal alteration assemblages with highest memberships appearing in the northeast and southwest corners of the study area. Figures 2 and 5 shows a noticeable congruence of the interpreted alteration areas with zones of mineral prospects and historic mines including Aburna mine and Tolegimja prospect, as well as with deposits of Anagulu, Aburna and Tolegimja. For example, the alterations with high membership values in all of the alterations as well as in zones of iron oxide - hydroxide minerals are aligned with the bimodal mafic Tolegimja Volcanogenic Massive Sulfide (VMS) deposit (yellow skew oval-shaped polygons) which represents the most recent deposit discovery (Figure 5). The location of monzonite / felsic intrusion hosted Anagulu porphyry corresponds with the enhanced zones of argillic, propylitic and silicic alterations, and with the zones of iron oxide-hydroxide minerals as shown in Figure 5. There is also a remarkable congruence of the shear hosted Aburna orogenic gold deposit with the zones accentuated as argillic alteration in Figure 5a. Furthermore, Figure 5 shows the proximal coexistence of the zones enhanced as iron oxide-hydroxide minerals with the other hydrothermal alterations.

Portrayal of these surface indicators can be further enhanced by assigning a false color classification image using red-green-blue (RGB) color composite from the SPCA images. The color composite provides a better platform for visualization and separation of similar spatial distributions associated with the presented alterations. The RGB false color image in Figure 6a is composed of fuzzified PC3 (argillic), PC2 (phyllic), and PC1(propylitic) alteration images shown in red, green and blue colors, respectively. Combination of the alterations are displayed in yellow (argillic and phyllic), cyan (green and blue) and magenta (argillic and propylitic).

Subsequently, it becomes evident that the red color represents advanced argillization, which is indicative of porphyry-epithermal deposits (Hedenquist and Taran, 2013; Khashgerel et al., 2008; Noori et al., 2019; Sillitoe, 2000; Watanabe et al., 1997). According to Mavrogonatos et al. (2018) advanced argillic alteration, or "lithocaps", are genetically linked with high sulphidation epithermal and porphyry systems, and often develop at shallow levels above PCD, e.g. Lepanto-Far Southeast, Philippines (Hedenquist et al., 1998) and Maricunga, Chile (Muntean and Einaudi, 2001). With this spatial contiguity lithocaps have been described in many porphyry-epithermal deposits and prospects, and along with occurrence of sericitic alteration zone (represented by phyllic alteration in this study), they mark the change from high-sulfidation epithermal to the porphyry environment, e.g. Hugo Dummett Au-Cu deposit in Mongolia (Khashgerel et al., 2008) and Rosia Poieni Cu deposit in Romania (Milu et al., 2004). Furthermore these lithocaps are commonly found overlying or overprinting earlier alteration styles in many porphyry systems and creates telescopic sequencing of alterations (Khashgerel et al., 2008).

The spatial arrangement (distal and proximal relationship) of hydrothermal alteration halos to a deposit can be direct evidence of interaction between intrusion related hydrothermal fluids with adjacent wall rocks. Such evidence can be determinant factor for identifying mineralized zones in porphyry deposit environments (Lowell and Guilbert, 1970a; Mavrogonatos et al., 2018; Salehi and Tangestani, 2018). Thus, locations like those in the study area where argillic, phyllic and propylitic are found in proximity to each other can be considered highly prospective and useful exploration technique for identifying undiscovered deposits. This is substantiated by the Anagulu Cu-Au porphyry deposit discovered in the southwestern corner of the study area, where phyllic, argillic and propylitic are contiguous. Similarly, the Tolegimja

VMS deposit located in the northeastern corner (highlighted as white color in Figure 6a) represents assemblage of these alterations, thus confirming the high prospectivity of zones with such alteration assemblage. A simplified Boolean overlay solution of all of the alterations as well as iron oxide-hydroxide minerals are shown in Figure 6b. The white color in the northeastern corner is composed of all of the above mineralization proxies, which makes that region highly prospective. Both figures highlight the spatial association of the proximity relationship between discovered deposits and mapped alterations, based on which several localities (outlined by black polygons in Figure 6b) are identified as highly prospective.

Moreover, the spatial relationship of surface oxidation, mineralization and hydrothermal alterations arrangements was further explored by additional RGB color composites of fuzzified PC triplets such as argillic, iron oxide-hydroxide, and phyllic PC images (Appendix C), and propylitic, iron oxide-hydroxide, and silicic PC images. The findings conform the prior observations that there is a major coexistence of iron oxide-hydroxide minerals with the other hydrothermal alterations and linkage of the surface oxidation with the hydrothermal alterations and mineralized zones. For instance, in this research the surface oxidation appears to coincide with the prospective zones identified from RGB composite of argillic, phyllic and propylitic, and the oxidation can be due to processes such as staining by the mineralizing hydrothermal fluids. As a result, this spatial proximity corroborates iron oxide-hydroxide minerals' linkage with hydrothermally altered rocks and mineralization, and refutes its possible genetic relationship with acid-alteration that is barren of mineralization as established by Atapour and Aftabi (2007).

Lineaments

The spatial distribution and density maps of lineaments are shown in Figure 7. In the figure, the hillshade model reveals different surface relief features and directions with overlaying lineaments (blue color) computed from shaded relief, slope and profile curvature derivatives. In Figure 7, it is clear that a higher assembly of lineaments is observed over regions with high rugged topography and complex geological settings while in the flat area lineaments are sparse and scattered in different directions. In addition, the figure shows lineaments (lines in red color) extracted by Hough Transform (HT) automated method for mapping lineaments (Argialas and Mavrantza, 2004). The HT is a feature extraction technique which identifies straight line segments from the computed lineament lines. The segments obtained through HT can be used as indicators of global description associated with the general trend of the lineaments. In this study, the direction of the HT segments is in sync with the alignment of the distribution of highly altered argillic, propylitic, and iron oxide – hydroxide minerals zones which is the northeast-southwest direction. This led to generalization of lineament trend in the study area to be in northeast-southwest.

The directional trend is also visible in the lineament density map in Figure 7b. The highest concentration of lineaments is in the northeastern and southwestern portion of the study area while the central portion is characterized by the lowest concentration. The rose diagram in Figure 7c summarizes the dominant azimuth directions and the frequency for the lineaments. The rose diagrams depicts that most of the general structural trend of the lineament frequency is between 0 and 90° with the greatest frequency (longest bar) of approximately 45°. In the diagram the frequency of the lineaments is organized by the length where dark green color depicts the longest lineament segments which are in the same 45° direction. Interestingly, the orientation of this directional trend is congruent to the general foliation of the study area which is between 30° and 50° (Alpha exploration, 2023). However, the mean direction (θ) from circular statistics is *theta* = 71.7° with a mean resultant length ($\bar{R}$) that is *rho* ≈ 0.635. The *rho* is a measure of concentration and indicates that all lineament directions are somewhat concentrated and point toward determined location. For instance, a *rho* value close to zero indicates a low concentration while a *rho* value close to one indicates that values are concentrated at a single location. The circular variance (V_m) which represents a measure of spread is $V_m = 0.365$, indicates to certain extent a higher concentration (i.e., low dispersion) of lineament directions. The circular variance represents one minus the mean resultant length and the interpretation is contrary to that of the mean resultant length.

Generally, the directional trend of the lineaments, and distribution of zones of high membership alterations and iron oxide-hydroxide minerals coincide in northeastern-southwestern direction. These also align with the northeastern-southwestern trend of mineralization in Anagulu, Aburna and Tolegimja deposits. Such observations indicate relationship of the lineaments with the mineralizing system, highlighting the link of the lineaments with genesis and spatial distribution of mineral deposits as well as signifying the lineament's role as fluid conduit to the mineralizing system. Additionally, these alignments generally coincide with the location of moderate to high-density lineament which spreads in northeastern-southwestern direction (Figure 7b). This relationship can be observed by juxtaposing maps of alterations (Figures 5 and 6), prospective zones (Figure 6) and lineament density (Figure 7b); however, there is also spatial relationship of low to moderate-density lineament zones with alterations, mineral deposits and prospective zones as observed in northeastern, eastern and southeastern corners of Figures 5, 6 and 7b. This latter observation clearly prevails in the zones of enhanced phyllic alteration (Figure

5b). Potentially this could be a manifestation of the colluvium overburden that concealed the underlying structures of the bedrocks and regolith. As a result, further investigation is required to indicate whether the alterations in the low lineament-density reflect an underlying mineralized body or transported material.

Results from Geochemical Data

The results from the PCA of the field-based geochemical data, which was transformed by CLR are presented in Table 4. The first ten PCs explained 84%, 83%, 82%, 83%, and 85% cumulative variances for argillic, phyllic, propylitic, silicic, and iron oxide-hydroxide minerals, respectively. Table 4 shows mineralization related PCs and pathfinder element associations that are grouped by zones of hydrothermal alterations and the iron oxide-hydroxide minerals. The PCs unrelated to mineralization were not included in the table. The table also summarizes the relationship of the selected PCs' loadings, variances, and variable assemblages and mineralization for each group. Besides, insights into the host rocks of the mineralization and type of hydrothermal deposit are given. For instance, in the argillic group, high negative loadings are associated with PC4 and PC5 which correspond to Au and Au-Cu mineralization, respectively. Moreover, PC5 exhibits high negative loading (contribution) of Au-Cu-P-S, which makes Cu-P-S pathfinder elements for Au. Another notable mineralization with the argillic alteration that is shown by high negative loadings is Zn mineralization in PC7, from which element association Pb-Cr-S-P are determined as Zn pathfinders. Further, the highest positive loadings in this PC signify Au mineralization along with similar high contribution of Ti-V in the PC, this relationship construes Ti-V as pathfinder elements for Au mineralization and the assemblage hints that the high positive loading of PC7 represent Au enriched mafic-metamafic rock. In the analysis of all of the PC loadings in each group (including PCs excluded from the table), it is observed that majority of the mineralization information is provided by the low variance PCs, while elemental assemblage that is descriptive of the lithology is often shown by high variance PCs (e.g., PC2 in Argillic and phyllic groups as well as PC3 in oxide-hydroxide minerals). Another important information extracted from the loadings in Table 4 is about deposit type, host rocks and mineralizing system: for example, loadings of PC4 and PC7 from phyllic and propylitic groups, respectively, indicated their association with lineaments, thus defining the Au mineralization in those PCs as shear (lineament) hosted orogenic deposit. Moreover, the host rocks and deposit types associated with the mineralizations in Table 4 are based on the pathfinder elements' potential source-lithologies, location and type of previously discovered deposits, and predicted spatial distribution of the mineralizations in the PCs.

The spatial implementation associated with the predicted PCs was explored by implementing inverse distance weighting (IDW) interpolation. For instance, Figure 8a was generated from PC5 using the argillic predictive model, and zones of high negative values that are associated with Au-Cu mineralization are shown as deep blue regions in the figure. This interpretation coincides spatially with the discoveries of Anagulu, Aburna and Tolegimja (Figure 5) which consolidates the interpretation of the concentric patches of deep blue colored regions in this PC5 as Au-Cu mineralized. Further this strengthens the alteration-based findings of this research that determined presence of PCD, VMS and orgonic Au in the study area.

Investigation on biplots of several pairs of mineralization-related PCs generated various element assemblages linked with Au, Cu and Zn mineralization. Variable vectors with lowest angular relationship with either of Au, Cu or Zn vectors were considered as the primary pathfinder elements linked to those mineralizations. For instance, in Figure 8b the primary pathfinder element of Au mineralization is V, which is identified by the matching directional vector angle of the Au and V vectors. Biplots in Appendix D also shows some pathfinder elements based on the matching directional vector angle: Appendix D (1) shows Y as pathfinder element of Au, and Appendix D (2) shows Zr and Ti as pathfinder elements of Au and Zn, respectively. Similarly, Appendix D (3) extracts the pathfinder association of Au and Ni, and the same biplot extracts As and S as pathfinders of Cu. In Appendix D (4), the pathfinder association of S with Au, Ni-Cr with Cu, and Ca with Zn are shown. After investigating several biplot possibilities, the identified pathfinder elements in Argillic setting are *a)* Cu-S-Y-Zr-Ni-V-Pb-Zn-P-Ti (±Cr) for Au mineralization, *b)* Zn-As-Ti-S-Nb-Cr-Zn-P-Ni (±Fe) for Cu mineralization and *c)* Ti-As-Cu-Ca-Pb-Zr-Y (±Mn, Mg and P) for Zn mineralization. Thus, several pathfinder element associations are generated for each of the mineralization; some of these pathfinder elements were not previously elucidated using loadings of single PCs (Table 4). Table 5 summarizes these pathfinder element assemblages. In addition, similar analysis of vector-to-vector angular relationship of the variables in those biplots extracted information about existence of lineament (shear) hosted orogenic Au deposits in phyllic setting**.** This coincides with the previous findings of loading-based analysis that showed PCs (Table 4) manifesting association of Au with lineament variable. Further, this coincidence also conforms with Aburna orogenic Au deposit. Hence, the lineament variable is an important predictor for orogenic Au deposit.

Results of biplot analysis using the first pairs of PCs in all of the alterations and iron oxide-hydroxide settings have also been assessed. In all of the settings the different lithologies of the study area were represented on either side of the corresponding PC1, while some were also plotted on either side of their corresponding PC2; however, PC1 did not account for any mineralized or alteration related lithologies. On the other hand, PC2 represented few mineralization and alteration related rocks in addition to accounting for unmineralized lithologies. These observations agree with the idea that the first two PCs carry lithology information, however the investigations proves that the second PC also contain information related to mineral deposits and mineralization related alterations.

Anomaly Detection by OCSVM and Validation

The spatial aggregation of categorical anomalous surface maps produced by majority and minority rules are shown in Figure 9. The OCSVM classifier was used to apply iterative thresholding to each PCA predicted map using the *nu* parameter (i.e., 0.05, 0.20, 0.40, 0.60, and 0.80). While the intention of the majority rule is to depict the dominant classes which become more pronounced, the minority rule depicts the rare classes. Indeed, implementation of both rules highlights similar spatial patterns which are also associated with the anomalies of Au-Cu-Zn. In the figure, the anomalous proportion of 5 % is represented by a dark green color. The relationship between the existing location of mines (n=18) that are overlaid on the anomalous surface maps in Figure 9 and the anomaly classes was validated by Pearson χ^2 test using cross-table approach. The χ^2 test with 360 observations and 5 degrees of freedom (*d.f.*) had a significant p-value < 0.001 which substantiates the alternative hypothesis (i.e., there is statistically significant association between the majority classes and presence-absence of mines). For the reported p-value that was associated with all six classes, the χ^2 statistics that was generated by using simulation (2,000 replicates) had a total of 16.7 % of the cells with expected value below 5. However, regrouping the classes into three groups (0 – 40%, 40 – 80%, 80-100%) met the assumption and yielded also a significant p-value of < 0.001.

Furthermore, the box plots in Figure 10 show the summary of variable distributions from the majority rule that were separated into anomalous (5 %) and non-anomalous areas. The standardized *z*-scores in the figure are especially useful for understanding the differences between and within the distributions of anomalous and non-anomalous observations. For example, in Figure 10, the *z*-scores of Nb and Pb in the anomalous group are higher by several magnitudes of SD than the *z*-scores of the same elements in the non-anomalous group. Another comparison between anomalous and non-anomalous soil geochemical samples using the raw ppm scores of Au, Cu, and Zn are shown in Figure 11. The figure shows that the median values of Au and Zn are, expectedly, greater in the anomalous zone while the median value for Cu is lower in the anomalous zone. Potentially this lower median value of Cu could be a manifestation of the presence of a PCD that was previously identified in this research using hydrothermal alteration analyses. Characteristically PCD are known by low-grade (low concentration)-high tonnage Cu concentration, and this low Cu concentration in PCD could be the reason for Cu's low median in the anomalous zone. Also, the differences between the anomalous and non-anomalous groups were tested by the K-W test. The statistics obtained from the K-W were $\chi^2 = 26.41$ and p-value < 0.01 for Au, $\chi^2 = 55.56$ and p-value < 0.01 for Cu, and $\chi^2 = 181.78$ and p-value < 0.01 for Zn which suggest that there are significant differences between values from anomalous and non-anomalous areas.

CONCLUSION

Accurate MPM is a difficult task due to complex geological dynamics associated with mineralization processes. To tackle this challenge, the presented study demonstrated an integrative approach of multispectral ASTER sensor, DEM, and soil geochemistry datasets applied in the Kerkesha region, southwestern Eritrea. In the proposed approach, first the smaller target areas with possible mineral deposits were delineated by SPCA using spectral information from ASTER, which is a sensor with effective ability for mapping hydrothermal alterations in the initial steps of mineral exploration. However, to better understand the occurrence of particular hydrothermal alteration minerals and to increase the reliability with the interpreted hydrothermal alteration zones, the PCA was applied to the field collected geochemical data and the lineaments extracted from the DEM. The delineated alteration zones and the zones of iron oxide - hydroxide minerals were used to train the PCA, while the predictions were applied to the entire study area. Lastly, to highlight anomalies of Au-Cu-Zn, OCSVM thresholding-based classification was used in conjunction with spatial aggregation performed by minority and majority rules. The K-W test was used to evaluate the significance between anomalous and non-anomalous groups, while Pearson's Chi-square test evaluated the association between known mineral deposits and predicted anomalous areas.

The spatial integration of different datasets provided comprehensive results regarding the occurrence of particular hydrothermal alterations attributable to multiple mineralizing systems. Interpretation of these alterations added PCD-epithermal deposits to the long-standing idea and practice of relating Eritrea's part of ANS to VMS and orogenic Au. The interpretation of hydrothermal alteration zones and pathfinder elements associated with the known mineral deposits can be used as first step to prioritize areas for mineral exploration. In addition, the importance of the application of predictive modeling in identifying Au-Cu-Zn pathfinder elements and mineralized zones as well as application of OCSVM in delineating anomalous zones shows promising results for robust automated mineral exploration.

However, future efforts and model improvement could be explored by versatile and integrative multivariate datasets that are generated by newer multispectral and hyperspectral RS platforms and field spectral analysis. Implementation of automated algorithms such as various ML classifiers, feature extraction, data fusion, anomaly detecting deep learning approaches can also catapult MPM into elevated level of exploration and subsequent improvements especially for swift identification of mineralized zones and classification of bedrock geology covered by transported overburden. In addition, integrative approaches as presented here can be of great scientific importance for highlighting depositional environment or mineralizing system.

REFERENCES

Abd El Monsef, M., Slobodník, M., Salem, I.A., 2018. Hydrothermal evolution of granitoid-hosted gold mineralization in gidami area: An example for orogenic-gold deposits in Egypt. Journal of African Earth Sciences, Precambrian Geology of Egypt: Stratigraphy, Geodynamics, and Mineral Resources 146, 132–149. https://doi.org/10.1016/j.jafrearsci.2018.04.007

Abdelsalam, M.G., Stern, R.J., Berhane, W.G., 2000. Mapping gossans in arid regions with Landsat TM and SIR-C images: the Beddaho Alteration Zone in northern Eritrea. Journal of African Earth Sciences 30, 903–916. https://doi.org/10.1016/S0899-5362(00)00059-2

Abrams, 1999. ASTER User Handbook.

Abrams, M., 2000. The Advanced Spaceborne Thermal Emission and Reflection Radiometer (ASTER): data products for the high spatial resolution imager on NASA's Terra platform. international Journal of Remote sensing 21, 847–859.

Abrams, M., Hook, S.J., 1995. Simulated ASTER data for geologic studies. IEEE Transactions on Geoscience and remote sensing 33, 692–699.

Afzal, P., Mirzaei, M., Yousefi, M., Adib, A., Khalajmasoumi, M., Zarifi, A.Z., Foster, P., Yasrebi, A.B., 2016. Delineation of geochemical anomalies based on stream sediment data utilizing fractal modeling and staged factor analysis. Journal of African Earth Sciences 119, 139–149. https://doi.org/10.1016/j.jafrearsci.2016.03.009

Aitchison, J., 1986. The Statistical Analysis of Compositional Data. Journal of the Royal Statistical Society: Series B (Methodological) 44, 139–160. https://doi.org/10.1111/j.2517-6161.1982.tb01195.x

Aliyari, F., Rastad, E., Zengqian, H., 2007. Orogenic Gold Mineralization in the Qolqoleh Deposit, Northwestern Iran. Resource Geology 57, 269–282. https://doi.org/10.1111/j.1751-3928.2007.00022.x

Alpha exploration, 2023. Alpha exploration [WWW Document].

Andersson, U.B., Ghebreab, W., Teklay, M., 2006. Crustal evolution and metamorphism in east-central Eritrea, south-east Arabian-Nubian Shield. Journal of African Earth Sciences 44, 45–65. https://doi.org/10.1016/j.jafrearsci.2005.11.006

Argialas, D.P., Mavrantza, O.D., 2004. Comparison of edge detection and Hough transformation techniques for the extraction of geologic features 34.

Atapour, H., Aftabi, A., 2007. The geochemistry of gossans associated with Sarcheshmeh porphyry copper deposit, Rafsanjan, Kerman, Iran: Implications for exploration and the environment. Journal of Geochemical Exploration 93, 47–65. https://doi.org/10.1016/j.gexplo.2006.07.007

Balaram, V., Sawant, S.S., 2022. Indicator minerals, pathfinder elements, and portable analytical instruments in mineral exploration studies. Minerals 12, 394.

Barrie, C.T., Abdalla, M.A.F., Hamer, R.D., 2016. Volcanogenic Massive Sulphide–Oxide Gold Deposits of the Nubian Shield in Northeast Africa, in: Bouabdellah, M., Slack, J.F. (Eds.), Mineral Deposits of North Africa, Mineral Resource Reviews. Springer International Publishing, Cham, pp. 417–435. https://doi.org/10.1007/978-3-319-31733-5_17

Barrie, C.T., Nielsen, F.W., Aussant, C.H., 2007. The Bisha volcanic-associated massive sulfide deposit, western Nakfa terrane, Eritrea. Economic Geology 102, 717–738.

Bedell, R.L., 2001. Geological mapping with ASTER satellite: new global satellite data that is a significant leap in remote sensing geologic and alteration mapping. Special Publication Geology Society of Nevada 33, 329–334.

Berhe, S.M., 1990. Ophiolites in Northeast and East Africa: implications for Proterozoic crustal growth. Journal of the Geological Society 147, 41–57.

Bierlein, F.P., McKeag, S., Reynolds, N., Bargmann, C.J., Bullen, W., Murphy, F.C., Al-Athbah, H., Brauhart, C., Potma, W., Meffre, S., McKnight, S., 2016. The Jebel Ohier deposit—a newly discovered porphyry copper–gold system in the Neoproterozoic Arabian–Nubian Shield, Red Sea Hills, NE Sudan. Miner Deposita 51, 713–724. https://doi.org/10.1007/s00126-015-0630-z

Bierlein, F.P., Potma, W., Cernuschi, F., Brauhart, C., Robinson, J., Bargmann, C.J., Bullen, W., Henriquez, J.F., Davies, I., Kennedy, A., 2020. New Insights into the Evolution and Age of the Neoproterozoic Jebel Ohier Porphyry Copper Deposit, Red Sea Hills, Northeastern Sudan. Economic Geology 115, 1–31. https://doi.org/10.5382/econgeo.4691

Burrough, P.A., McDonnell, R.A., Lloyd, C.D., 2015. Principles of geographical information systems. Oxford university press.

Camilli, G., Hopkins, K.D., 1978. Applicability of chi-square to 2 × 2 contingency tables with small expected cell frequencies. Psychological Bulletin 85, 163–167. https://doi.org/10.1037/0033-2909.85.1.163

Cardoso Fonseca, E., Martin, H., 1986. The selective extraction of Pb and Zn in selected mineral and soil samples, application in geochemical exploration (Portugal). Journal of Geochemical Exploration 26, 231–248. https://doi.org/10.1016/0375-6742(86)90074-9

Carranza, E.J.M., 2011. Analysis and mapping of geochemical anomalies using logratio-transformed stream sediment data with censored values. Journal of Geochemical Exploration 110, 167–185.

Carranza, E.J.M., Laborte, A.G., 2015. Data-driven predictive mapping of gold prospectivity, Baguio district, Philippines: Application of Random Forests algorithm. Ore Geology Reviews 71, 777–787. https://doi.org/10.1016/j.oregeorev.2014.08.010

Cattell, R.B., 1966. The Scree Test for The Number Of Factors. Multivariate Behavioral Research 1, 245–276. https://doi.org/10.1207/s15327906mbr0102_10

Chang, Z., Hedenquist, J.W., White, N.C., Cooke, D.R., Roach, M., Deyell, C.L., Garcia, J., Jr, Gemmell, J.B., McKnight, S., Cuison, A.L., 2011. Exploration Tools for Linked Porphyry and Epithermal Deposits: Example from the Mankayan Intrusion-Centered Cu-Au District, Luzon, Philippines*. Economic Geology 106, 1365–1398. https://doi.org/10.2113/econgeo.106.8.1365

Chen, X.-W., Lin, X., 2014. Big data deep learning: challenges and perspectives. IEEE access 2, 514–525.

Chen, Y., Lu, L., Li, X., 2014. Application of continuous restricted Boltzmann machine to identify multivariate geochemical anomaly. Journal of Geochemical Exploration 140, 56–63. https://doi.org/10.1016/j.gexplo.2014.02.013

Chen, Y., Wu, W., 2019. Isolation Forest as an Alternative Data-Driven Mineral Prospectivity Mapping Method with a Higher Data-Processing Efficiency. Nat Resour Res 28, 31–46. https://doi.org/10.1007/s11053-018-9375-6

Chen, Y., Wu, W., 2017. Application of one-class support vector machine to quickly identify multivariate anomalies from geochemical exploration data. Geochemistry: Exploration, Environment, Analysis 17, 231–238.

Chisambi, J., Haundi, T., Tsokonombwe, G., 2021. Geologic structures associated with gold mineralization in the Kirk Range area in Southern Malawi. Open Geosciences 13, 1345–1357. https://doi.org/10.1515/geo-2020-0304

Crosta, A.P., De Souza Filho, C.R., Azevedo, F., Brodie, C., 2003. Targeting key alteration minerals in epithermal deposits in Patagonia, Argentina, using ASTER imagery and principal component analysis. International journal of Remote sensing 24, 4233–4240.

Crosta, A.P., Moore, J.M., 1989. Rehancement of LANDSAT Thematic Mapper imagery for residual soil mapping in SW Minas Gerais State, Brazil: A prospecting case history in Greenstone Belt terrain. Presented at the Thematic conference on remote sensing for exploration geology. Methods, integration, solutions. 7, pp. 1173–1187.

Crowley, J.K., Brickey, D.W., Rowan, L.C., 1989. Airborne imaging spectrometer data of the Ruby Mountains, Montana: Mineral discrimination using relative absorption band-depth images. Remote Sensing of Environment 29, 121–134. https://doi.org/10.1016/0034-4257(89)90021-7

Diaz, L.R., Santos, D.C., Käfer, P.S., Rocha, N.S. da, Costa, S.T.L. da, Kaiser, E.A., Rolim, S.B.A., 2021. Atmospheric Correction of Thermal Infrared Landsat Images Using High-Resolution Vertical Profiles Simulated by WRF Model. Environmental Sciences Proceedings 8, 27. https://doi.org/10.3390/ecas2021-10351

Drury, S.A., Berhe, S.M., 1993. Accretion tectonics in northern Eritrea revealed by remotely sensed imagery. Geological Magazine 130, 177–190. https://doi.org/10.1017/S0016756800009845

Drury, S.A., De Souza Filho, C.R., 1998. Neoproterozoic terrane assemblages in Eritrea: review and prospects. Journal of African Earth Sciences 27, 331–348. https://doi.org/10.1016/S0899-5362(98)00066-9

Dubé, B., Gosselin, P., Mercier-Langevin, P., Hannington, M., Galley, A., 2007. Gold-rich volcanogenic massive sulphide deposits. Geological Association of Canada, Mineral Deposits Division 75–94.

El-Desoky, H.M., Soliman, N., Heikal, M.A., Abdel-Rahman, A.M., 2021. Mapping hydrothermal alteration zones using ASTER images in the Arabian–Nubian Shield: A case study of the northwestern Allaqi District, South Eastern Desert, Egypt. Journal of Asian Earth Sciences: X 5, 100060.

Filzmoser, P., Hron, K., Reimann, C., 2009. Principal component analysis for compositional data with outliers. Environmetrics: The Official Journal of the International Environmetrics Society 20, 621–632.

Fisher, L., Gazley, M.F., Baensch, A., Barnes, S.J., Cleverley, J., Duclaux, G., 2014. Resolution of geochemical and lithostratigraphic complexity: a workflow for application of portable X-ray fluorescence to mineral exploration. Geochemistry: Exploration, Environment, Analysis 14, 149–159. https://doi.org/10.1144/geochem2012-158

Fritz, H., Abdelsalam, M., Ali, K.A., Bingen, B., Collins, A.S., Fowler, A.R., Ghebreab, W., Hauzenberger, C.A., Johnson, P.R., Kusky, T.M., Macey, P., Muhongo, S., Stern, R.J., Viola, G., 2013. Orogen styles in the East African Orogen: A review of the

Neoproterozoic to Cambrian tectonic evolution. Journal of African Earth Sciences 86, 65–106. https://doi.org/10.1016/j.jafrearsci.2013.06.004

Gale, G.H., 2003. Vectoring volcanogenic massive sulphide deposits using rare earth elements and other pathfinder elements at the Ruttan mine, Manitoba (NTS 63B5). Report of activities 54–73.

Galvão, L.S., Almeida-Filho, R., Vitorello, Í., 2005. Spectral discrimination of hydrothermally altered materials using ASTER short-wave infrared bands: Evaluation in a tropical savannah environment. International Journal of Applied Earth Observation and Geoinformation 7, 107–114. https://doi.org/10.1016/j.jag.2004.12.003

Gazley, M., Hood, S.B., Cracknell, M.J., 2021. Soil-sample geochemistry normalised by class membership from machine-learnt clusters of satellite and geophysics data. Ore Geology Reviews 139, 104442. https://doi.org/10.1016/j.oregeorev.2021.104442

Gazley, M.F., Caciagli, N., Hood, S.B., McFarlane, A., 2019. Multivariate data analysis and machine learning – towards robust geometallurgical domains: examples from the Pacific Rim. New Zealand 3.

Gazley, M.F., Fisher, L.A., 2014. A review of the reliability and validity of portable X-ray fluorescence spectrometry (pXRF) data. Mineral resource and ore reserve estimation–The AusIMM guide to good practice 69, 82.

Ghebreab, W., Greiling, R.O., Solomon, S., 2009. Structural setting of Neoproterozoic mineralization, Asmara district, Eritrea. Journal of African Earth Sciences 55, 219–235.

Gorsevski, P.V., Jankowski, P., Gessler, P.E., 2006. An heuristic approach for mapping landslide hazard by integrating fuzzy logic with analytic hierarchy process. Control and Cybernetics 35, 121–146.

Govett, G.J.S., Goodfellow, W.D., Chapman, R.P., Chork, C.Y., 1975. Exploration geochemistry—Distribution of elements and recognition of anomalies. Mathematical Geology 7, 415–446. https://doi.org/10.1007/BF02080498

Grunsky, E.C., 2010. The interpretation of geochemical survey data. GEEA 10, 27–74. https://doi.org/10.1144/1467-7873/09-210

Grunsky, E.C., 1986. Recognition of alteration in volcanic rocks using statistical analysis of lithogeochemical data. Journal of Geochemical Exploration 25, 157–183. https://doi.org/10.1016/0375-6742(86)90012-9

Grunsky, E.C., Caritat, P. de, 2019. State-of-the-art analysis of geochemical data for mineral exploration. Geochemistry: Exploration, Environment, Analysis 20, 217–232. https://doi.org/10.1144/geochem2019-031

Grunsky, E.C., Mueller, U.A., Corrigan, D., 2014. A study of the lake sediment geochemistry of the Melville Peninsula using multivariate methods: applications for predictive geological mapping. Journal of Geochemical Exploration 141, 15–41.

Hale, M., 1981. Pathfinder Applications of Arsenic, Antimony and Bismuth in Geochemical Exploration, in: Rose, A.W., Gundlach, H. (Eds.), Developments in Economic Geology, Geochemical Exploration 1980. Elsevier, pp. 307–323. https://doi.org/10.1016/B978-0-444-42012-1.50024-6

Harris, J.R., Rencz, A.N., Ballantyne, B., Sheridon, C., 1998. Mapping altered rocks using LANDSAT TM and lithogeochemical data: Sulphurets-Brucejack Lake district, British Columbia, Canada. Photogrammetric engineering and remote sensing 64, 309–322.

Harsanyi, J.C., Chang, C.-, 1994. Hyperspectral image classification and dimensionality reduction: an orthogonal subspace projection approach. IEEE Transactions on Geoscience and Remote Sensing 32, 779–785. https://doi.org/10.1109/36.298007

Hawkes, H.E., Webb, J.S., 1963. Geochemistry in Mineral Exploration. Soil Science 95, 283.

Hedenquist, J., Taran, Y., 2013. Modeling the Formation of Advanced Argillic Lithocaps: Volcanic Vapor Condensation Above Porphyry Intrusions. Economic Geology 108, 1523–1540. https://doi.org/10.2113/econgeo.108.7.1523

Hedenquist, J.W., Arribas, A., Reynolds, T.J., 1998. Evolution of an intrusion-centered hydrothermal system; Far Southeast-Lepanto porphyry and epithermal Cu-Au deposits, Philippines. Economic Geology 93, 373–404. https://doi.org/10.2113/gsecongeo.93.4.373

Honarmand, M., Ranjbar, H., Shahabpour, J., 2012. Application of Principal Component Analysis and Spectral Angle Mapper in the Mapping of Hydrothermal Alteration in the Jebal–Barez Area, Southeastern Iran. Resource Geology 62, 119–139. https://doi.org/10.1111/j.1751-3928.2012.00184.x

Hood, S.B., Cracknell, M.J., Gazley, M.F., Reading, A.M., 2019. Improved supervised classification of bedrock in areas of transported overburden: Applying domain expertise at Kerkasha, Eritrea. Applied Computing and Geosciences 3–4, 100001. https://doi.org/10.1016/j.acags.2019.100001

Hron, K., Templ, M., Filzmoser, P., 2010. Imputation of missing values for compositional data using classical and robust methods. Computational Statistics & Data Analysis 54, 3095–3107. https://doi.org/10.1016/j.csda.2009.11.023

Johnson, P.R., Andresen, A., Collins, A.S., Fowler, A.R., Fritz, H., Ghebreab, W., Kusky, T., Stern, R.J., 2011. Late Cryogenian–Ediacaran history of the Arabian–Nubian Shield: a review of depositional, plutonic, structural, and tectonic events in the closing stages of the northern East African Orogen. Journal of African Earth Sciences 61, 167–232.

Johnson, P.R., Zoheir, B.A., Ghebreab, W., Stern, R.J., Barrie, C.T., Hamer, R.D., 2017. Gold-bearing volcanogenic massive sulfides and orogenic-gold deposits in the Nubian Shield. South African Journal of Geology 120, 63–76. https://doi.org/10.25131/gssajg.120.1.63

Jolliffe, I., 2011. Principal component analysis (pp. 1094-1096). Springer Berlin Heidelberg. RESUME SELİN DEĞİRMECİ Marmara University, Goztepe Campus ProQuest Number: ProQuest). Copyright of the Dissertation is held by the Author. All Rights Reserved 28243034, 28243034.

Kadel-Harder, I.M., Spry, P.G., McCombs, A.L., Zhang, H., 2021. Identifying pathfinder elements for gold in bulk-rock geochemical data from the Cripple Creek Au–Te deposit: a statistical approach. GEEA 21, geochem2020-048. https://doi.org/10.1144/geochem2020-048

Kaiser, H.F., 1960. The application of electronic computers to factor analysis. Educational and psychological measurement 20, 141–151.

Khashgerel, B.-E., Kavalieris, I., Hayashi, K., 2008. Mineralogy, textures, and whole-rock geochemistry of advanced argillic alteration: Hugo Dummett porphyry Cu–Au deposit, Oyu Tolgoi mineral district, Mongolia. Mineralium Deposita 43, 913–932.

Kruse, F.A., Lefkoff, A.B., Boardman, J.W., Heidebrecht, K.B., Shapiro, A.T., Barloon, P.J., Goetz, A.F.H., 1993. The spectral image processing system (SIPS)—interactive visualization and analysis of imaging spectrometer data. Remote sensing of environment 44, 145–163.

Kwarteng, P., Chavez, A., 1989a. Extracting spectral contrast in Landsat Thematic Mapper image data using selective principal component analysis. Photogramm. Eng. Remote Sens 55, 339–348.

Kwarteng, P., Chavez, A., 1989b. Extracting spectral contrast in Landsat Thematic Mapper image data using selective principal component analysis. Photogramm. Eng. Remote Sens 55, 339–348.

Livo, K.E., Clark, R.N., Knepper, D.H., 1993. SPVIEW; spectral plot program for accessing the USGS Digital Spectral Library database with MS-DOS personal computers, version 1.00. Open-File Report. https://doi.org/10.3133/ofr93593A

Loughlin, W.P., 1991. Principal component analysis for alteration mapping. Photogrammetric Engineering and Remote Sensing 57, 1163–1169.

Lowell, J.D., Guilbert, J.M., 1970a. Lateral and vertical alteration-mineralization zoning in porphyry ore deposits. Economic geology 65, 373–408.

Mars, J.C., Rowan, L.C., 2006. Regional mapping of phyllic- and argillic-altered rocks in the Zagros magmatic arc, Iran, using Advanced Spaceborne Thermal Emission and Reflection Radiometer (ASTER) data and logical operator algorithms. Geosphere 2, 161–186. https://doi.org/10.1130/GES00044.1

Martín-Fernández, J.A., Hron, K., Templ, M., Filzmoser, P., Palarea-Albaladejo, J., 2012. Model-based replacement of rounded zeros in compositional data: Classical and robust approaches. Computational Statistics & Data Analysis 56, 2688–2704. https://doi.org/10.1016/j.csda.2012.02.012

Masoumi, F., Eslamkish, T., Honarmand, M., Abkar, A.A., 2017. A Comparative Study of Landsat-7 and Landsat-8 Data Using Image Processing Methods for Hydrothermal

Alteration Mapping: Landsat 7/8 for Hydrothermal Alteration Mapping. Resource Geology 67, 72–88. https://doi.org/10.1111/rge.12117

Mavrogonatos, C., Voudouris, P., Spry, P.G., Melfos, V., Klemme, S., Berndt, J., Baker, T., Moritz, R., Bissig, T., Monecke, T., 2018. Mineralogical study of the advanced argillic alteration zone at the Konos Hill Mo–Cu–Re–Au porphyry prospect, NE Greece. Minerals 8, 479.

Milu, V., Milesi, J.-P., Leroy, J.L., 2004. Rosia Poieni copper deposit, Apuseni Mountains, Romania: Advanced argillic overprint of a porphyry system. Mineralium Deposita 39, 173–188.

Mojeddifar, S., Ranjbar, H., Nezamabadi-pour, H., 2013. Adaptive Neuro-Fuzzy Inference System application for hydrothermal alteration mapping using ASTER data 4, 83–96.

Muntean, J.L., Einaudi, M.T., 2001. Porphyry-Epithermal Transition: Maricunga Belt, Northern Chile. Economic Geology 96, 743–772. https://doi.org/10.2113/gsecongeo.96.4.743

Ndossi, M.I., Avdan, U., 2016. Inversion of Land Surface Temperature (LST) Using Terra ASTER Data: A Comparison of Three Algorithms. Remote Sensing 8, 993. https://doi.org/10.3390/rs8120993

Ninomiya, Y., 2003. A stabilized vegetation index and several mineralogic indices defined for ASTER VNIR and SWIR data, International Geoscience and Remote Sensing Symposium (IGARSS). https://doi.org/10.1109/IGARSS.2003.1294172

Noori, L., Pour, A.B., Askari, G., Taghipour, N., Pradhan, B., Lee, C.-W., Honarmand, M., 2019. Comparison of different algorithms to map hydrothermal alteration zones using ASTER remote sensing data for polymetallic vein-type ore exploration: Toroud–Chahshirin Magmatic Belt (TCMB), North Iran. Remote Sensing 11, 495.

Nude, P.M., Asigri, J.M., Yidana, S.M., Arhin, E., Foli, G., Kutu, J.M., 2012. Identifying Pathfinder Elements for Gold in Multi-Element Soil Geochemical Data from the Wa-Lawra Belt, Northwest Ghana: A Multivariate Statistical Approach. International Journal of Geosciences 3, 62–70. https://doi.org/10.4236/ijg.2012.31008

Ostertagová, E., Ostertag, O., Kováč, J., 2014. Methodology and Application of the Kruskal-Wallis Test. Applied Mechanics and Materials 611, 115–120. https://doi.org/10.4028/www.scientific.net/AMM.611.115

Pearson, N.C., Livo, K.E., Driscoll, R.L., Lowers, H.A., Hoefen, T.M., Swayze, G.A., Klein, A.J., Kokaly, R.F., Wise, R.A., Benzel, W.M., Clark, R.N., 2017. USGS Spectral Library Version 7 Data. https://doi.org/10.5066/F7RR1WDJ

Perelló, J., Brockway, H., García, A., 2020. A minimum Thanetian (Paleocene) age for the African Surface in the Eritrean highlands, Northeast Africa. Journal of African Earth Sciences 164, 103782. https://doi.org/10.1016/j.jafrearsci.2020.103782

Perry, J.L., Vincent, R.K., 2009. ASTER Brightness and Ratio Codes for Minerals: Application to Lithologic Mapping in the West-Central Powder River Basin, Wyoming¤, in: Bedell, R., Crósta, A.P., Grunsky, E. (Eds.), Remote Sensing and Spectral Geology. Society of Economic Geologists, p. 0. https://doi.org/10.5382/Rev.16.12

Pour, A.B., Hashim, M., 2012. The application of ASTER remote sensing data to porphyry copper and epithermal gold deposits. Ore Geology Reviews 44, 1–9. https://doi.org/10.1016/j.oregeorev.2011.09.009

Rajendran, S., Nasir, S., 2017. Characterization of ASTER spectral bands for mapping of alteration zones of volcanogenic massive sulphide deposits. Ore Geology Reviews 88, 317–335. https://doi.org/10.1016/j.oregeorev.2017.04.016

Rockwell, B.W., 2004. Spectral variations in rocks and soils containing ferric iron hydroxide and (or) sulfate minerals as seen by AVIRIS and laboratory spectroscopy. DIANE Publishing.

Rockwell, B.W., Hofstra, A.H., 2008. Identification of quartz and carbonate minerals across northern Nevada using ASTER thermal infrared emissivity data—Implications for geologic mapping and mineral resource investigations in well-studied and frontier areas. Geosphere 4, 218–246.

Rodriguez-Galiano, V., Sanchez-Castillo, M., Chica-Olmo, M., Chica-Rivas, M., 2015. Machine learning predictive models for mineral prospectivity: An evaluation of neural networks, random forest, regression trees and support vector machines. Ore Geology Reviews 71, 804–818.

Rowan, L.C., Mars, J.C., 2003. Lithologic mapping in the Mountain Pass, California area using Advanced Spaceborne Thermal Emission and Reflection Radiometer (ASTER) data. Remote Sensing of Environment 84, 350–366. https://doi.org/10.1016/S0034-4257(02)00127-X

Ruiz-Armenta, J.R., Prol-Ledesma, R.M., 1998. Techniques for enhancing the spectral response of hydrothermal alteration minerals in Thematic Mapper images of Central Mexico. International Journal of Remote Sensing 19, 1981–2000.

Sadeghi, M., Billay, A., Carranza, E.J.M., 2015. Analysis and mapping of soil geochemical anomalies: Implications for bedrock mapping and gold exploration in Giyani area, South Africa. Journal of Geochemical Exploration 154, 180–193. https://doi.org/10.1016/j.gexplo.2014.11.018

Safari, M., Maghsoudi, A., Pour, A.B., 2018. Application of Landsat-8 and ASTER satellite remote sensing data for porphyry copper exploration: a case study from Shahr-e-Babak, Kerman, south of Iran. Geocarto international 33, 1186–1201.

Salehi, T., Tangestani, M., 2018. Large-scale mapping of iron oxide and hydroxide minerals of Zefreh porphyry copper deposit, using Worldview-3 VNIR data in the Northeastern Isfahan, Iran. International Journal of Applied Earth Observation and Geoinformation 73, 156–169. https://doi.org/10.1016/j.jag.2018.06.010

Sander, M.V., Einaudi, M.T., 1990. Epithermal deposition of gold during transition from propylitic to potassic alteration at Round Mountain, Nevada. Economic Geology 85, 285–311. https://doi.org/10.2113/gsecongeo.85.2.285

Schölkopf, B., Platt, J.C., Shawe-Taylor, J., Smola, A.J., Williamson, R.C., 2001. Estimating the support of a high-dimensional distribution. Neural computation 13, 1443–1471.

Sekertekin, A., Arslan, N., 2019. Monitoring thermal anomaly and radiative heat flux using thermal infrared satellite imagery – A case study at Tuzla geothermal region. Geothermics 78, 243–254. https://doi.org/10.1016/j.geothermics.2018.12.014

Sheikhrahimi, A., Pour, A.B., Pradhan, B., Zoheir, B., 2019. Mapping hydrothermal alteration zones and lineaments associated with orogenic gold mineralization using ASTER data: A case study from the Sanandaj-Sirjan Zone, Iran. Advances in Space Research 63, 3315–3332. https://doi.org/10.1016/j.asr.2019.01.035

Sillitoe, R.H., 2010. Porphyry copper systems. Economic geology 105, 3–41.

Sillitoe, R.H., 2000. Styles of high-sulphidation gold, silver and copper mineralisation in porphyry and epithermal environments, in: Proceedings of the Australasian Institute of Mining and Metallurgy. Citeseer, pp. 19–34.

Sinclair, A.J., 1974. Selection of threshold values in geochemical data using probability graphs. Journal of Geochemical Exploration 3, 129–149. https://doi.org/10.1016/0375-6742(74)90030-2

Stern, R.J., 1994. Neoproterozoic (900-550 Ma) arc assembly and continental collision in the East Africa orogen: Implications for the consolidation of Gondwanaland. Annual Review of Earth and Planetary Sciences 22, 319–351.

Swayze, G.A., Smith, K.S., Clark, R.N., Sutley, S.J., Pearson, R.M., Vance, J.S., Hageman, P.L., Briggs, P.H., Meier, A.L., Singleton, M.J., Roth, S., 2000. Using Imaging Spectroscopy To Map Acidic Mine Waste. Environ. Sci. Technol. 34, 47–54. https://doi.org/10.1021/es990046w

Tangestani, M.H., Mazhari, N., Agar, B., 2005. Mapping the porphyry copper alteration zones at the Meiduk area, SE Iran, using the advanced spaceborne thermal emission and reflection radiometer (ASTER) data, in: Ehlers, M., Michel, U. (Eds.), . Presented at the Remote Sensing, Bruges, Belgium, p. 59830S. https://doi.org/10.1117/12.626505

Tayebi, M.H., Tangestani, M.H., Vincent, R.K., 2014. Alteration mineral mapping with ASTER data by integration of coded spectral ratio imaging and SOM neural network model. Turkish Journal of Earth Sciences 23, 627–644.

Teklay, M., 1997. Petrology, geochemistry and geochronology of Neoproterozoic magmatic arc rocks from Eritrea: implications for crustal evolution in the southern Nubian Shield. Department of Mines-Ministry of Energy Mines and Water Resources-State of ….

Templ, M., Filzmoser, P., Reimann, C., 2008. Cluster analysis applied to regional geochemical data: Problems and possibilities. Applied Geochemistry 23, 2198–2213. https://doi.org/10.1016/j.apgeochem.2008.03.004

Templ, M., Hron, K., Filzmoser, P., 2011. robCompositions: An R-package for Robust Statistical Analysis of Compositional Data, in: Compositional Data Analysis. John Wiley & Sons, Ltd, pp. 341–355. https://doi.org/10.1002/9781119976462.ch25

Testa, F.J., Villanueva, C., Cooke, D.R., Zhang, L., 2018. Lithological and Hydrothermal Alteration Mapping of Epithermal, Porphyry and Tourmaline Breccia Districts in the Argentine Andes Using ASTER Imagery. Remote Sensing 10, 203. https://doi.org/10.3390/rs10020203

USGS, 2020. ASTER USGS GUIDLINE AST LT.

Vincent, R.K., 1997. Fundamentals of geological and environmental remote sensing. Prentice Hall.

Wang, J., Zhou, Y., Xiao, F., 2020. Identification of multi-element geochemical anomalies using unsupervised machine learning algorithms: A case study from Ag–Pb–Zn deposits in north-western Zhejiang, China. Applied Geochemistry 120, 104679.

Wang, J., Zuo, R., 2022. Model averaging for identification of geochemical anomalies linked to mineralization. Ore Geology Reviews 104955.

Watanabe, Y., AOKI, M., YAMAMOTO, K., 1997. Geology, age and style of the advanced argillic alteration in the Kobui area, Southwestern Hokkaido. Shigen-Chishitsu 47, 263–281.

Woldehaimanot, B., 2000. Tectonic setting and geochemical characterisation of Neoproterozoic volcanics and granitoids from the Adobha Belt, northern Eritrea. Journal of African Earth Sciences 30, 817–831. https://doi.org/10.1016/S0899-5362(00)00054-3

Xiong, Y., Zuo, R., 2020. Recognizing multivariate geochemical anomalies for mineral exploration by combining deep learning and one-class support vector machine. Computers & Geosciences 140, 104484.

Xiong, Y., Zuo, R., 2016. Recognition of geochemical anomalies using a deep autoencoder network. Computers & Geosciences 86, 75–82.

Yousefi, M., Kamkar-Rouhani, A., Carranza, E.J.M., 2014. Application of staged factor analysis and logistic function to create a fuzzy stream sediment geochemical evidence layer for mineral prospectivity mapping. Geochemistry: Exploration, Environment, Analysis 14, 45–58. https://doi.org/10.1144/geochem2012-144

Zadeh, L.A., 1965. Fuzzy sets. Information and Control 8, 338–353. https://doi.org/10.1016/S0019-9958(65)90241-X

Zekri, H., Cohen, D.R., Mokhtari, A.R., Esmaeili, A., 2019. Geochemical Prospectivity Mapping Through a Feature Extraction–Selection Classification Scheme. Nat Resour Res 28, 849–865. https://doi.org/10.1007/s11053-018-9422-3

Zhang, S., Xiao, K., Carranza, E.J.M., Yang, F., Zhao, Z., 2019. Integration of auto-encoder network with density-based spatial clustering for geochemical anomaly detection for mineral exploration. Computers & Geosciences 130, 43–56.

Zuo, R., Carranza, E.J.M., Wang, J., 2016. Spatial analysis and visualization of exploration geochemical data. Earth-Science Reviews 158, 9–18. https://doi.org/10.1016/j.earscirev.2016.04.006

Zuo, R., Xiong, Y., Wang, J., Carranza, E.J.M., 2019. Deep learning and its application in geochemical mapping. Earth-science reviews 192, 1–14.

APPENDIX A. FIGURES

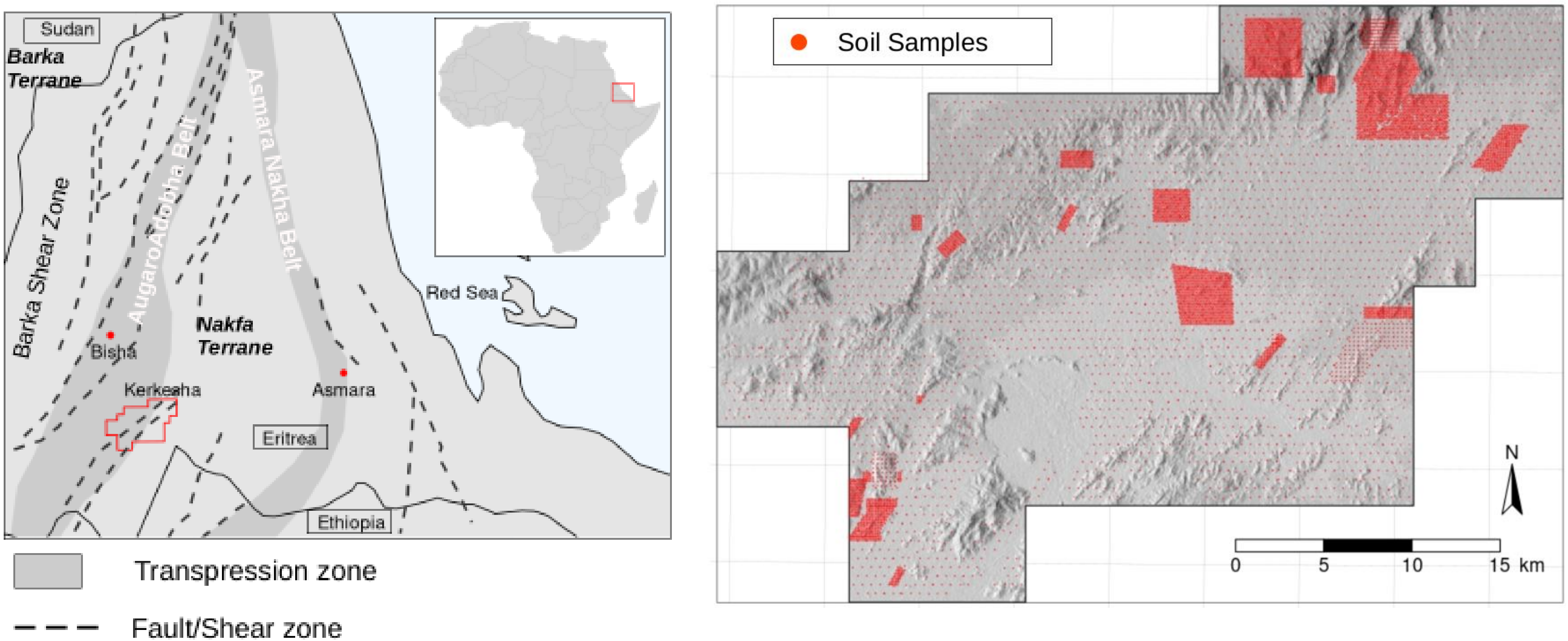

Figure 1. Study area: *a*) along with regional terranes, shear / fault zones and transpressional zones (modified from Gazley et al., 2021; Johnson et al., 2017a) and b) a hillshade of Kerkesha with location of soil samples in concentric red points representing prospect scale sample points while the rest represent regional scale samples.

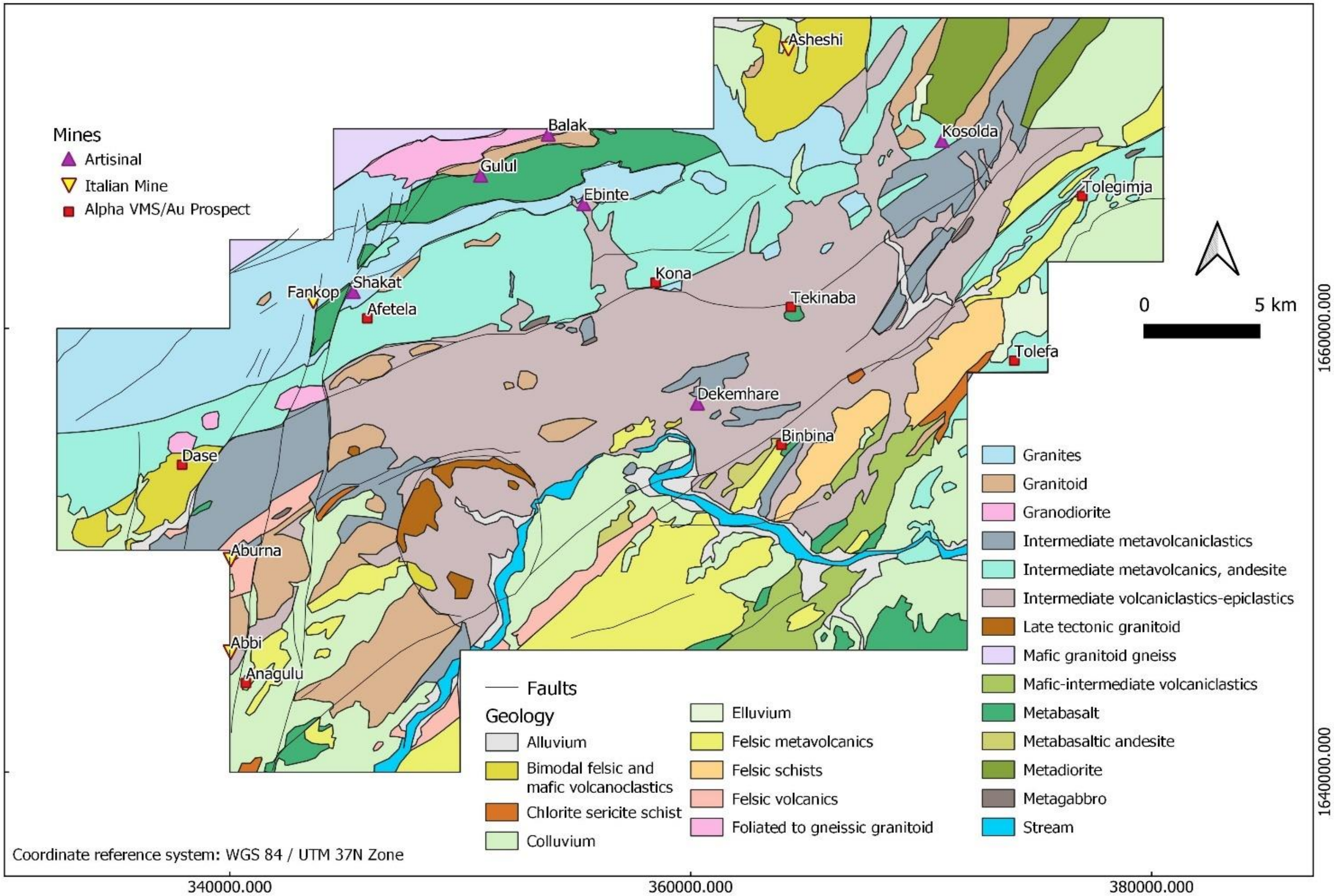

Figure 2. Geology and mineralization of study area (modified from Alpha exploration, 2023). The legend shows lithology, fault, prospects and historic mines.

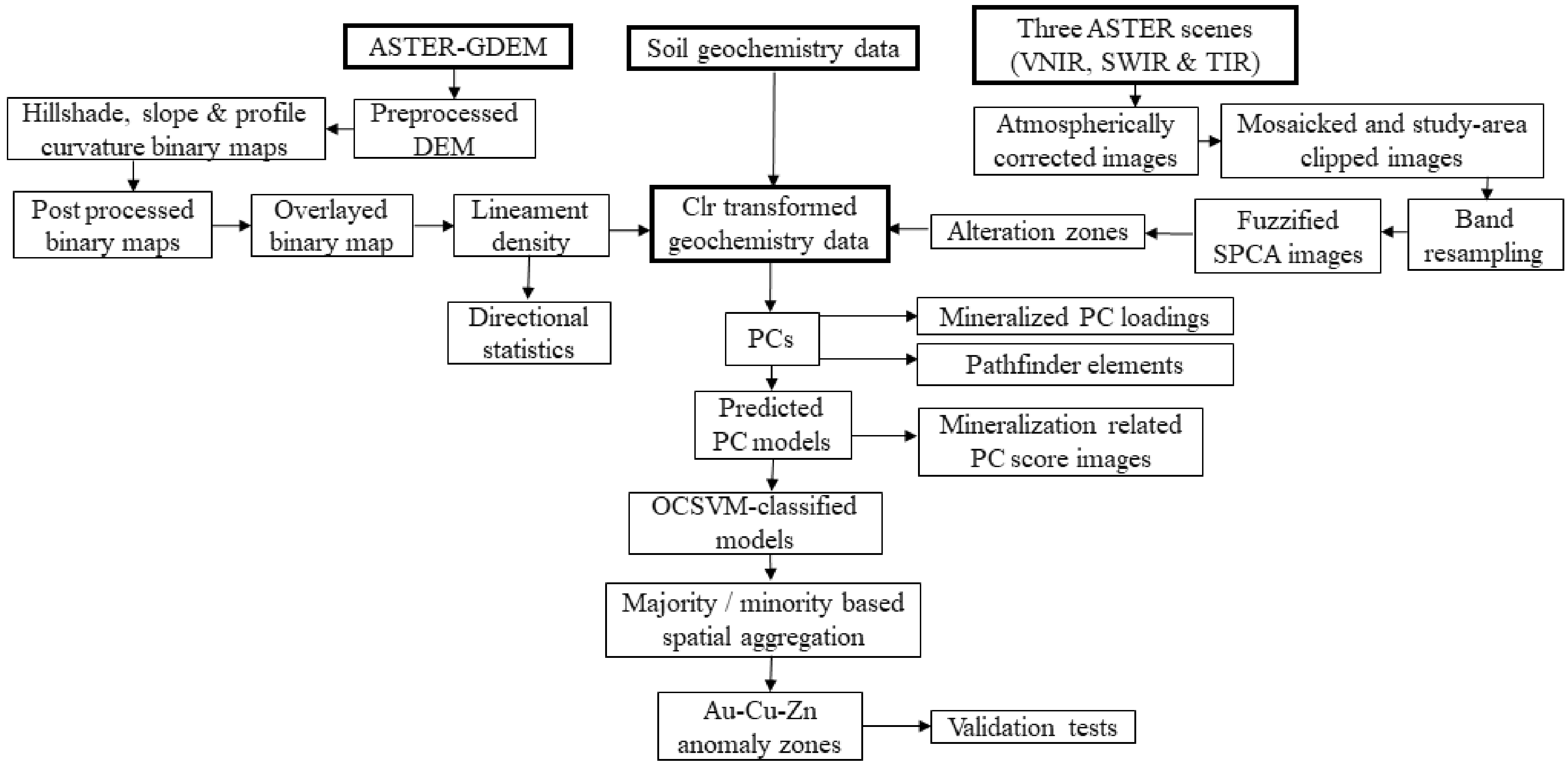

Figure 3. Flowchart of the methodology

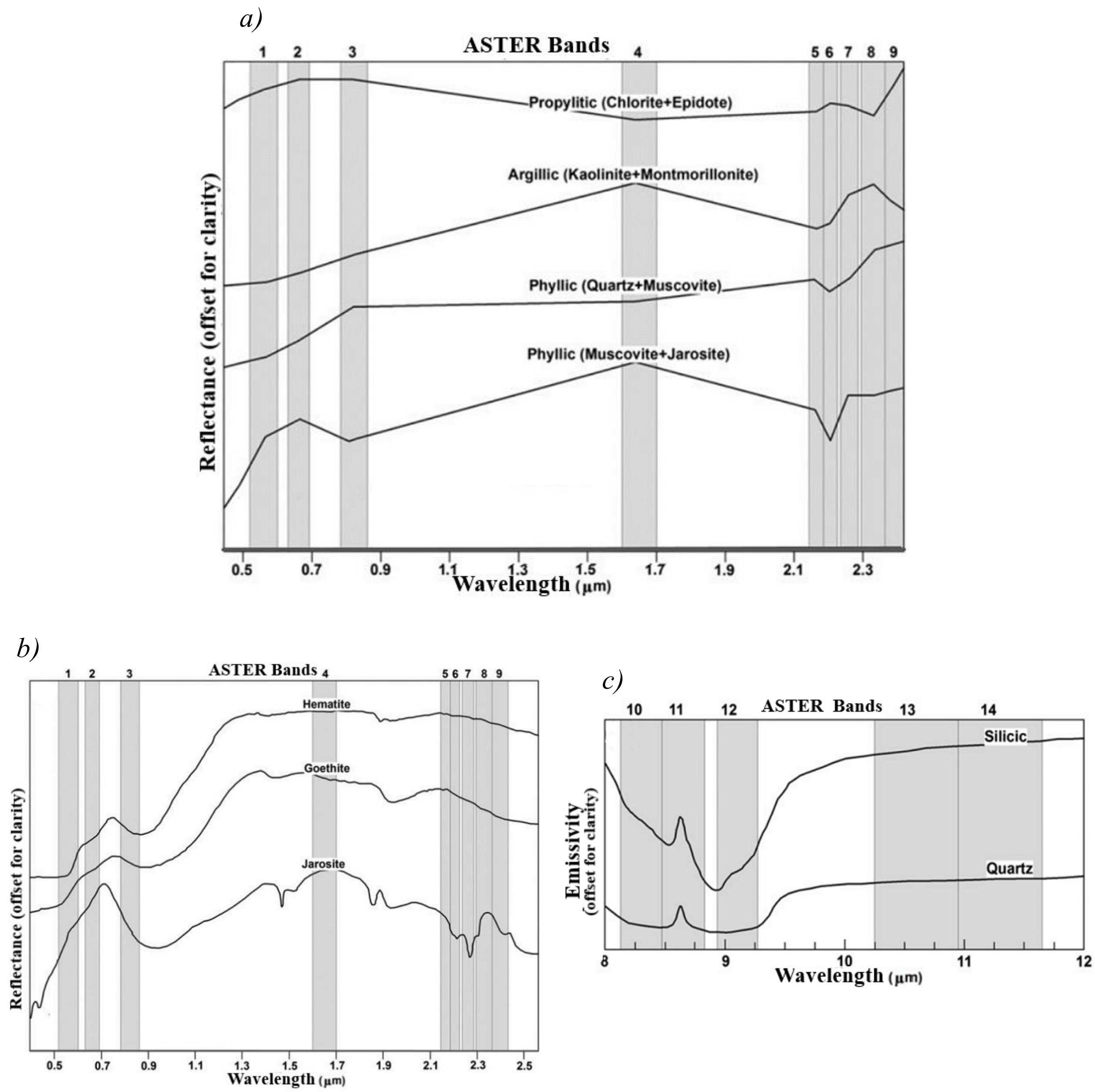

Figure 4. Spectral profiles of alterations and minerals in ASTER *a)* pixel spectral profile of four alteration zones, each profile represents the main constituents for each alteration zone, modified after Honarmand et al. (2012); *b)* spectral profiles of iron oxide – hydroxide minerals from USGS library (Livo et al., 1993); and *c)* laboratory emissivity spectra of quartz with emissivity spectra of silicic alteration, modified after Honarmand et al. (2012).

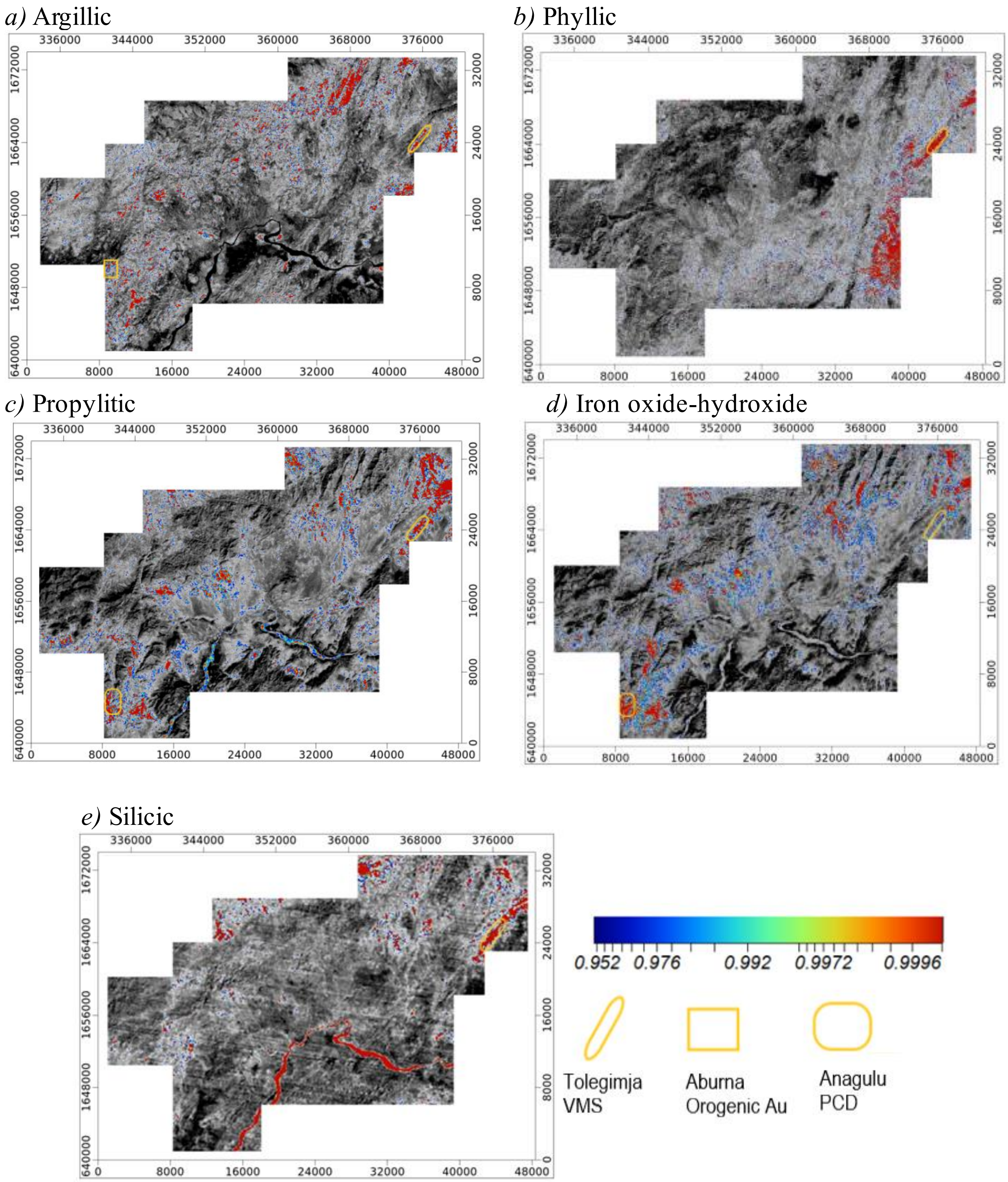

Figure 5. SPCA-based images with colorized prospective zones derived from fuzzified and thresholded PC images of *a)* argillic alteration, *b) p*hyllic alterations, *c)* propylitic alterations, *d)* iron oxide - hydroxide minerals, and *e)* silicic alteration; red region shows highest degree of membership. Yellow polygons depict new deposit discovery in the study area (Alpha exploration, 2023).

a) b)

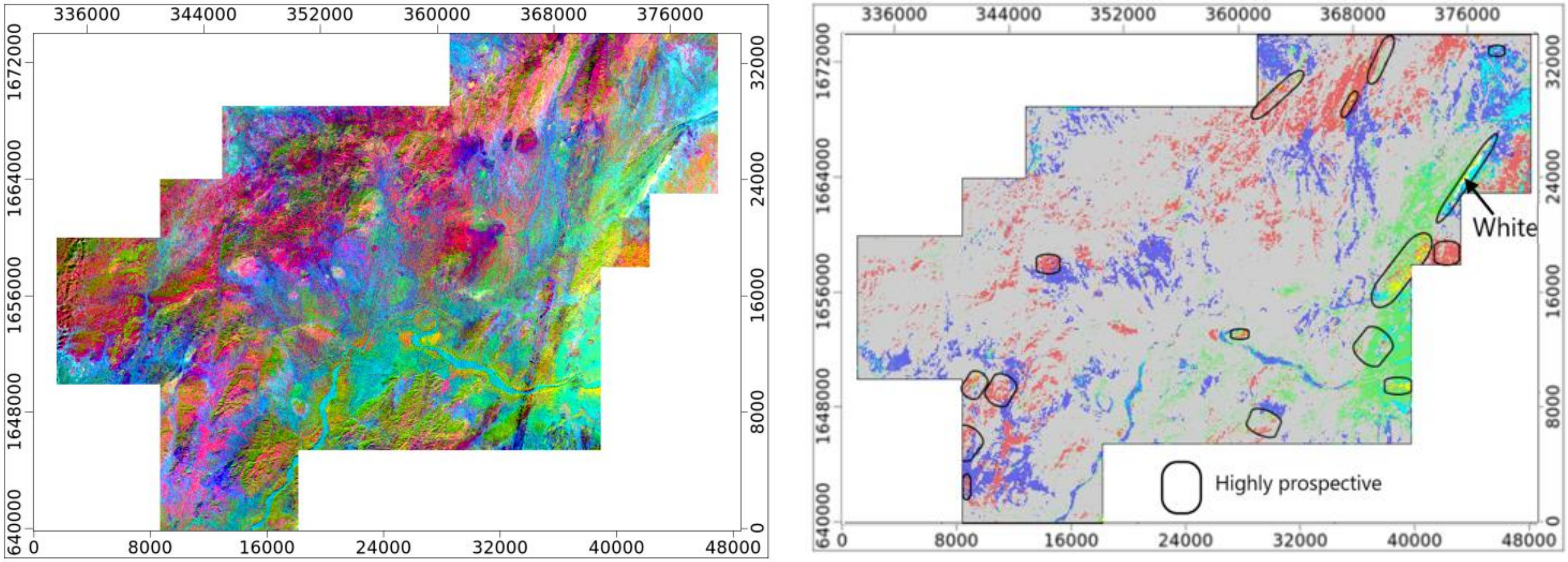

Figure 6. Images from fuzzified PCs derived by SPCA analysis: a*)* represents the RGB composite of argillic (R), phyllic (G) and propylitic alterations, and *b)* represents the simplified solution of the overlaid binary images (i.e., thresholded fuzzified PCs) that were identified as highly prospective zones; to pronounce the enhancement, 40% transparency is applied which caused the appearance of light shade of red and blue colors: black polygons show zones of high prospectivity. The polygon labelled white refers to the zone where all the alterations and iron oxide-hydroxide minerals exist.

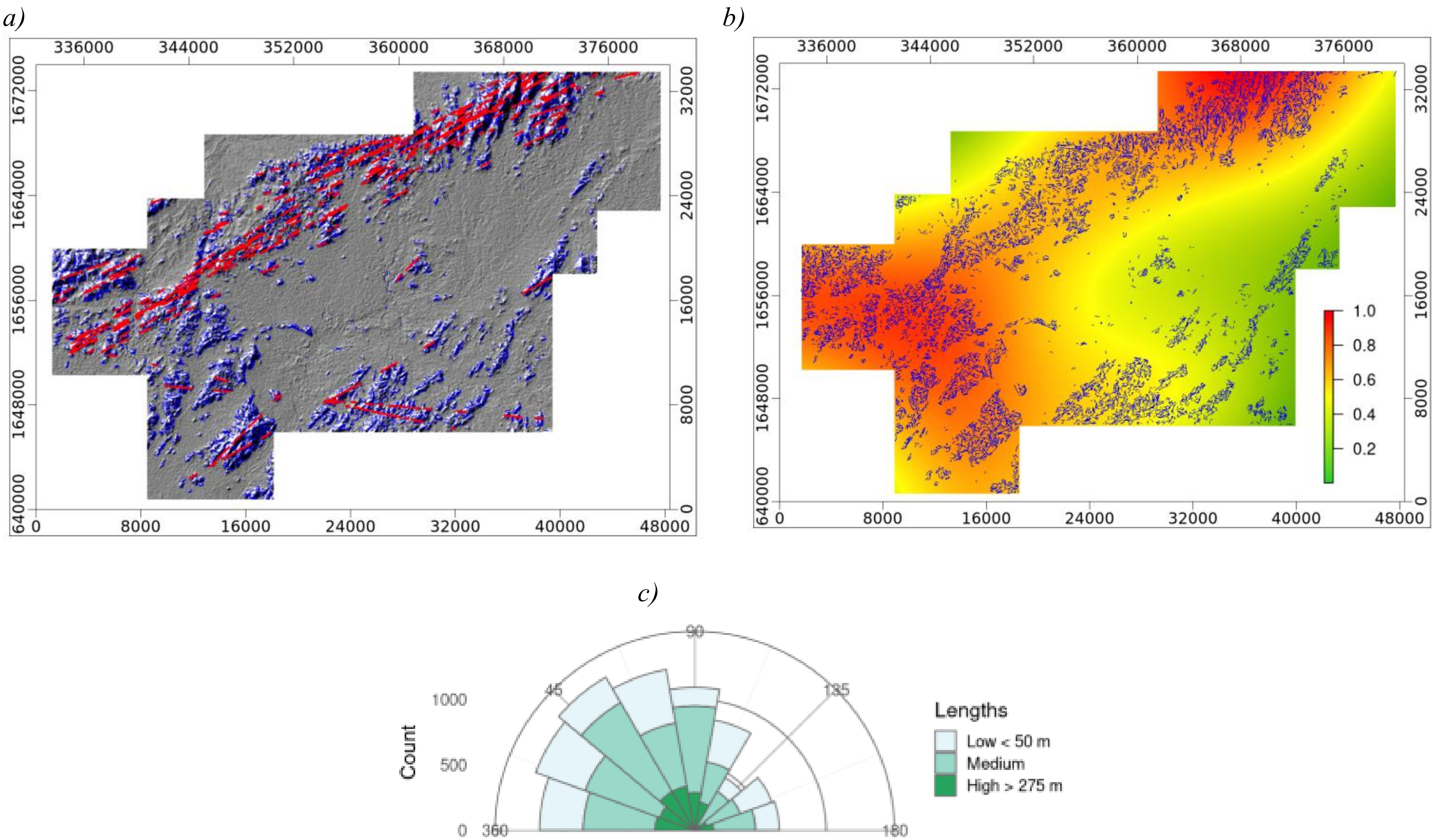

Figure 7. Lineaments derived from terrain attributes using different light source azimuths, slope and profile curvature *a)* distribution of lineaments (blue color) with overlayed Hough Transformation that reveals the general trends (dashed red color lines), b*)* lineament density map with rescaled values between 0 and 1, and c*)* half side of rose diagram that shows the angle directions and the frequency of the lineaments organized by lengths.

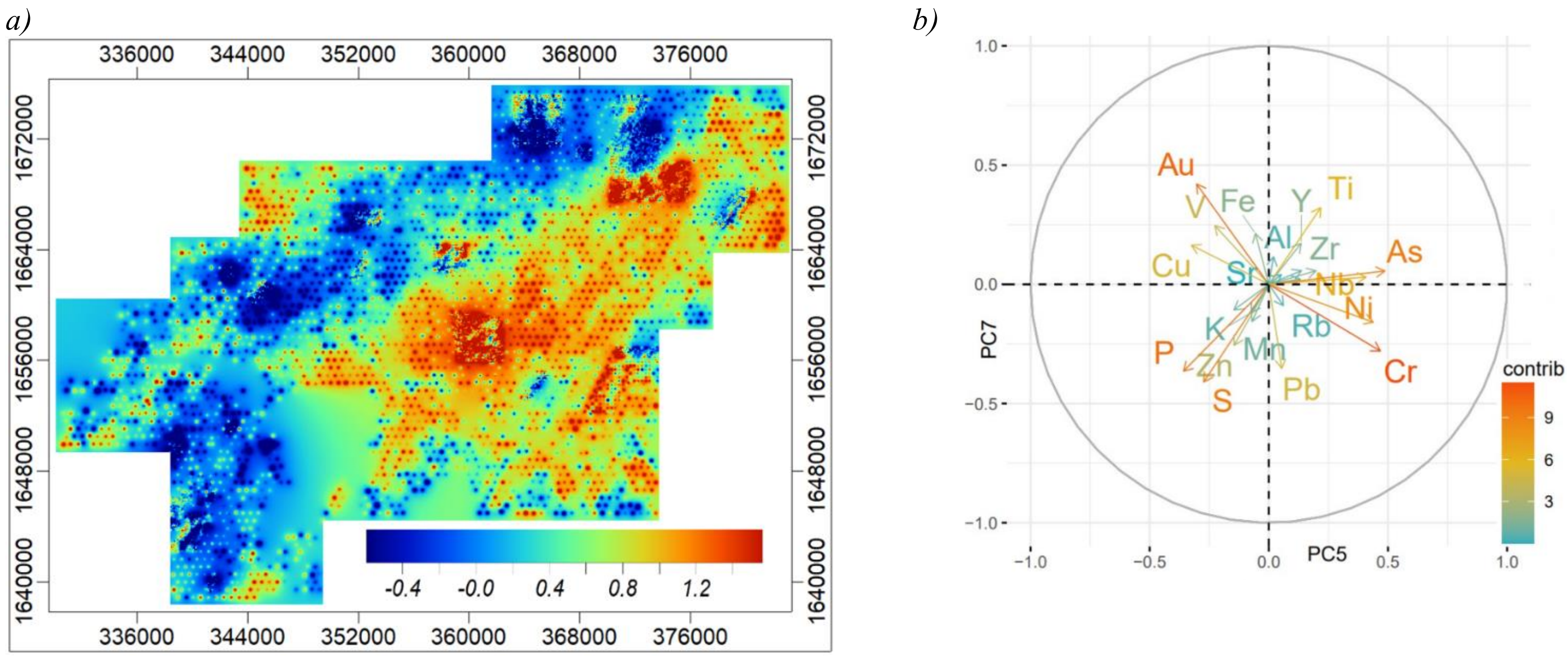

Figure 8. Example of the results generated by PCA using the argillic predictive model were *a)* IDW interpolation from PC5 is representative of Au and Cu mineralization (dense deep blue color), and *b)* is the biplot of PC5 and PC7 with high Au loadings: showing directional alignment and low angle relationship between Au and V vectors, while the graduated color scheme of the vectors indicating the vector's degree of contribution along PC5 and PC7 axes. The deep orange color of Au stands for its high contribution in b oth PCs.

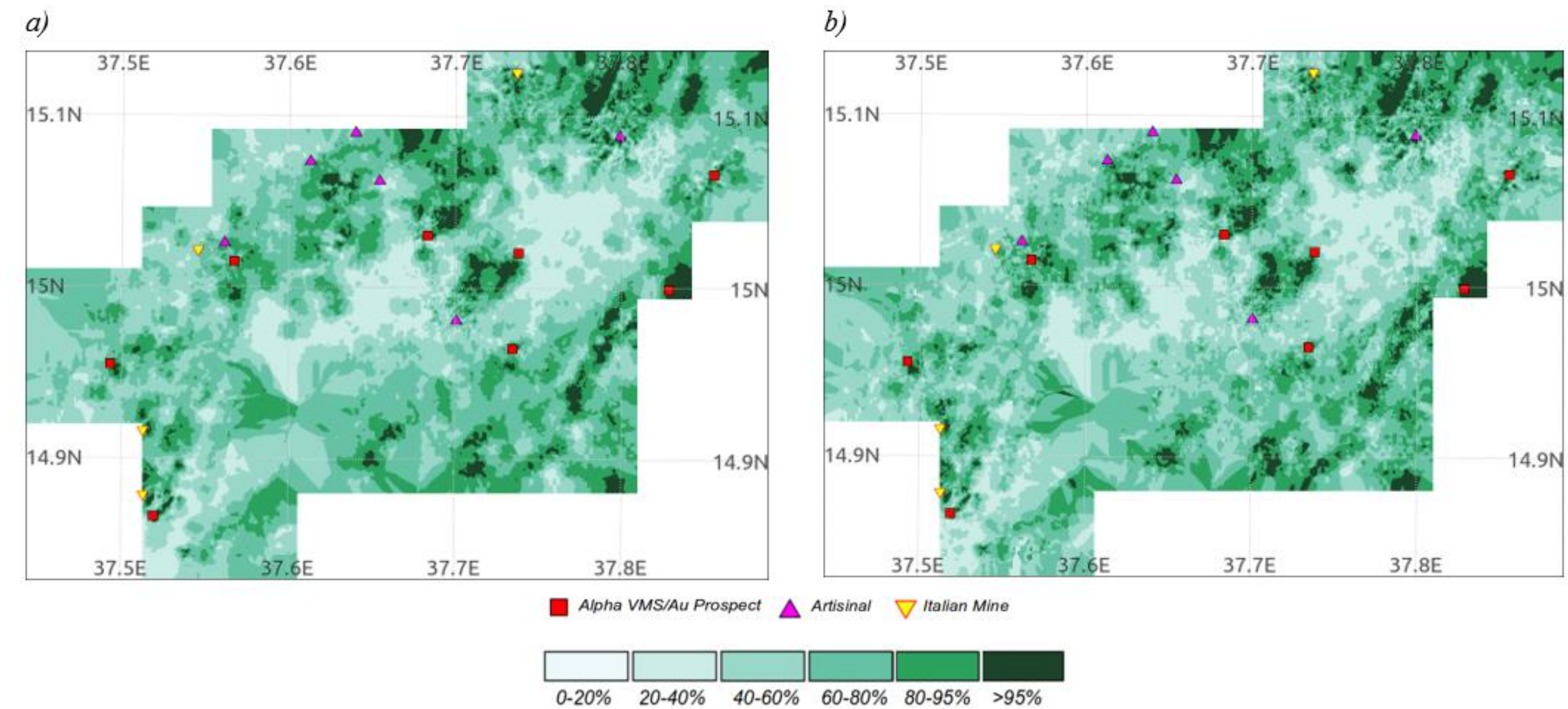

Figure 9. The spatially aggregated anomaly maps were derived by *a)* majority and *b)* minority rules using interpolated surfaces from PCs of field-based clr-transformed geochemical data which was subjected to multi-classification OCSVM unsupervised approach. The locations of historic mines, prospects / discoveries are overlayed and were used for validation: the tests validated the high anom aly classification, and zones in the class of > 95 % are highly prospective.

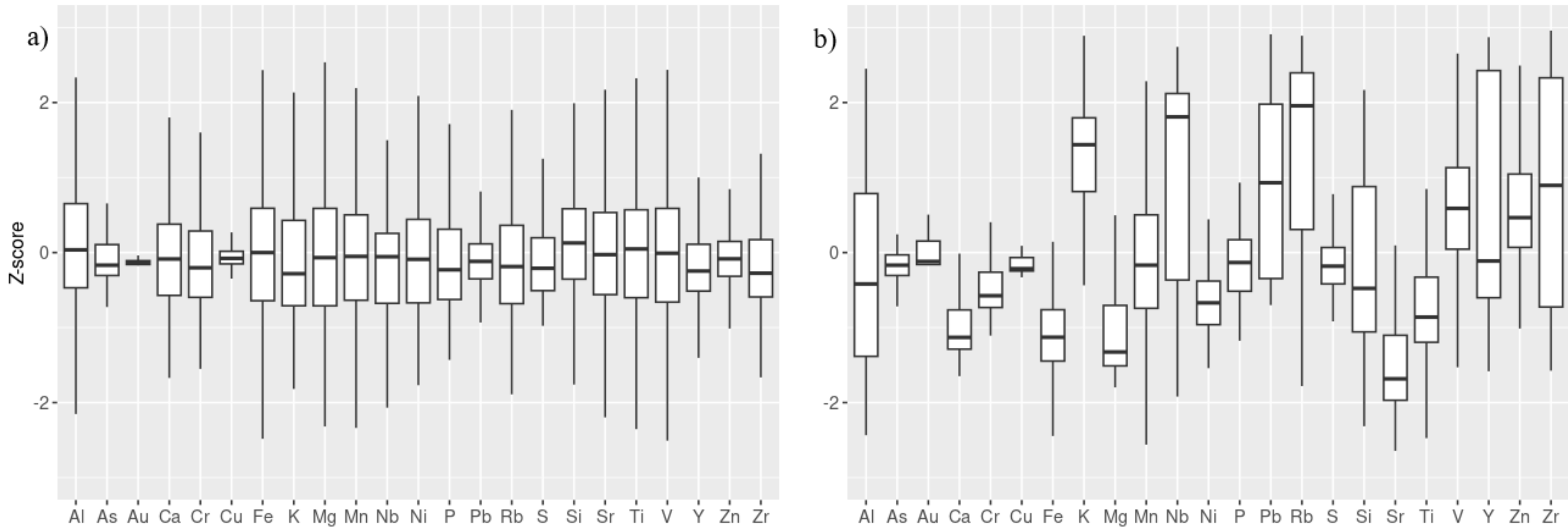

Figure 10. Boxplots which show comparison of z-score distributions from the soil geochemical dataset that was separated into *a)* non-anomalous and *b)* anomalous subsets. For the visualization, the majority rule was used to generate the two subsets where anomalous subset is represented by the areas associated with class '> 95 %' and non-anomalous otherwise.

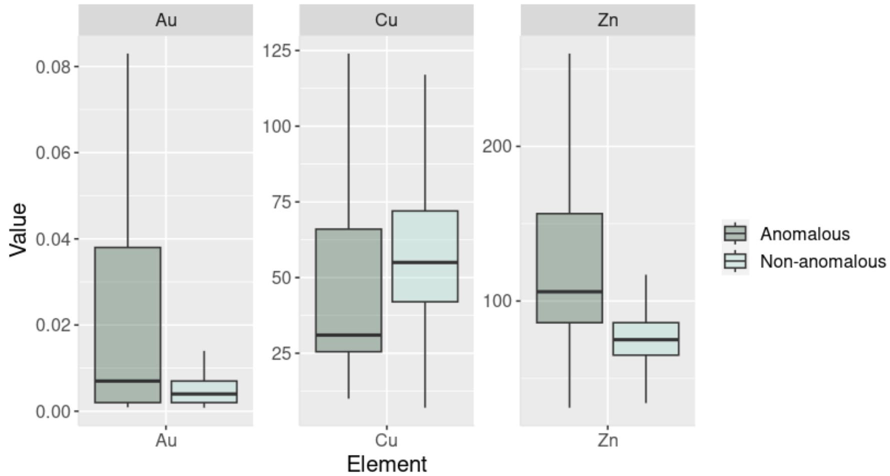

Figure 11. Comparison between anomalous and non-anomalous soil geochemical samples associated with Au, Cu, and Zn. The majority anomaly map was used to separate the anomalous from non-anomalous samples based on class '> 95 %' and '<= 95 %'.

APPENDIX B. TABLES

Table 1. ASTER spectral bands, spectral range, resolutions and bit depth (Abrams, 1999).

Sub system	Band Number	Spectral range (µm)	Spatial resolution(m)	Radiometric resolution
VNIR	1	0.52-0.60	15	8 bits
VNIR	2	0.63-0.69	15	8 bits
VNIR	3N	0.78-0.86	15	8 bits
VNIR	3B	0.78-0.86	15	8 bits
SWIR	4	1.6-1.7	30	8 bits
SWIR	5	2.145-2.185	30	8 bits
SWIR	6	2.185-2.225	30	8 bits
SWIR	7	2.235-2.285	30	8 bits
SWIR	8	2.295-2.365	30	8 bits
SWIR	9	2.360-2.430	30	8 bits
TIR	10	8.125-8.475	90	12 bits
TIR	11	8.475-8.825	90	12 bits
TIR	12	8.925-9.275	90	12 bits
TIR	13	10.25-10.95	90	12 bits
TIR	14	10.95-11.65	90	12 bits

Table 2. SPCA loadings in different settings: a) argillic, b) phyllic, c) propylitic, d) iron oxide-hydroxide minerals, and e) silicic.

a) Argillic

PC	Band4↑	Band5 ↓	Band6 ↓
PC1	-0.695169	-0.029991	-0.71822
PC2	-0.509663	-0.68403	0.521868
PC3	**-0.506935**	**0.728837**	**0.460231**

b) Phyllic

PC	Band5↑	Band6↓	Band7↑
PC1	-0.581729	0.334318	0.741501
PC2	**-0.576974**	**0.472955**	**-0.665893**
PC3	-0.573317	-0.815196	-0.082239

c) Propylitic

PC	Band7↑	Band8↓	Band9↓
PC1	**-0.754602**	**0.321908**	**0.571796**
PC2	-0.583429	0.069659	-0.809171
PC3	-0.30031	-0.944205	0.135246

d) iron oxide-hydroxide

PC	Band1↓	Band2↓	Band4↑
PC1	**0.300637**	**-0.48248**	**0.822697**
PC2	0.500295	-0.654617	-0.566729
PC3	0.811987	0.581971	0.04458

e) Silicic

PC	Band12↑	Band13↓	Band14↓
PC1	-0.566151	0.085984	-0.819805
PC2	-0.602327	-0.722114	0.340225
PC3	**-0.562739**	**0.68641**	**0.460616**

Table 3. Fuzzy control points

Alteration / Minerals	Control point a	Control point b	Fuzzy function / membership
Argillic	0.0105	0.0503	Sigmoidal curve - decreasing
Phyllic	0.0049	0.03	Sigmoidal curve - decreasing
Propylitic	-0.267	-0.089	Sigmoidal curve - decreasing
Iron oxide-hydroxide	0.059	0.318	Sigmoidal curve - increasing
Silicic	0.734	1.86	Sigmoidal curve - increasing

Table 4. Mineralization related PCs and pathfinder element association generated from loadings of the PCs.

Setting	PC	% Var.	Pathfinders	Load	Interpretation (Mineralization / host rock / deposit type)
Argillic	PC2	13.3	Au-Zn-Y-Zr-Pb	+	Au-Zn in granitoids
Argillic	PC3	8.3	Cu-Zn-As-Si-Al	+	Cu-Zn in felsic schist / metavolcanics
Argillic	PC4	7.6	-	-	Au in Felsic metavolcanics
Argillic	PC5	6.2	Au-Cu-P-S	-	Au-Cu in felsic metavolcanics; PCD & orogenic deposits
Argillic	PC7	4.7	Au-Ti-V	+	Au in mafics / metamafics; VMS & PCD
Argillic	PC7	4.7	Zn-Pb-Cr-S-P	-	Zn in mafics / metamafics
Argillic	PC8	4.3	Cu-P-Ti-Cr-Ni	+	Cu in mafics / metamafics
Phyllic	PC2	12.5	Cu-Zn-Y-Fe-Al-Si	-	Cu-Zn in felsic schist / metavolcanics & metamafics; VMS, PCD and orogenic
Phyllic	PC4	8.2	Au-Lineament	+	Shear hosted Au
Phyllic	PC8	4.4	Cu-Ti	-	Cu in in mafics / metamafics; VMS & orogenic deposits
Phyllic	PC9	4	Au-Ti-Fe-Y-Nb	-	Au in granitoid, metadiorite & metavolcanics
Propylitic	PC2	12.8	Cu-S	+	Cu in felsic volcanics / metavolcanics; PCD, VMS and orogenic
Propylitic	PC4	8.9	Au-Ni-Y-Nb	+	Au in granitoids, metadiorite & intermediate metavolcanics
Propylitic	PC5	6.6	Au	-	Au in felsic volcanics, and in metavolcanics / metavolcaniclastics / volcanics
Propylitic	PC7	4.7	Au-Zn-V-Mn-Fe-lineament	-	Shear hosted Au-Zn in metadiorite & felsic volcanics
Propylitic	PC8	4.1	Cu	-	Cu in felsic schist / metavolcanics & granitoids; PCD
Iron oxide-hydroxide	PC2	12.5	Au-Cu-S	+	Au-Cu in felsic volcanics / metavolcanics/ schist; VMS, PCD and orogenic deposits
Iron oxide-hydroxide	PC3	10.9	Au-Zn-Y	+	Au-Zn hosted in felsic shists / metavolcanics; VMS and PCD
Iron oxide-hydroxide	PC4	9.5	Cu-Al-Si	-	Cu in felsic shists/ metavolcanics / volcanics, granitoids; PCD, VMS and orogenic
Iron oxide-hydroxide	PC6	5.3	Au-Cu-Sr	-	Au-Cu in felsic shists/metavolcanics/ volcanics & granitoids; PCD, VMS and orogenic
Iron oxide-hydroxide	PC8	3.72	Au-V	+	Au in metadiorite & metavolcaniclastics / metavolcanics; Orogenic
Silicic	PC2	12.6	Au-S-Zn	-	Au in felsic volcanics / metavolcanics/ schist, granitoids & metavolcanics; VMS, PCD and orogenic
Silicic	PC6	5.3	Au-Pb	-	Au in felsic shist / metavolcanic; VMS & PCD
Silicic	PC8	3.8	Au	-	Au in felsic / intermediate volcanics; Orogenic
Silicic	PC10	2.8	Cu-S-Ti-V-Fe	+	Cu in metabasalt; PCD

Table 5. Mineralization-related pathfinder element associations in different alterations and iron oxide-hydroxide settings, generated from biplot pairing of several mineralization-related PCs.

Setting	Mineralization	Pathfinder element assemblage
Argillic	Au	Cu-S-Y-Zr-Ni-V-Pb-Ti-Zn-P-Ti (±Cr)
Argillic	Cu	As-Ti-S-Nb-Cr-Zn-P-Ni (±Fe)
Argillic	Zn	Ti-As-Cu-Ca-Pb-Zr-Y (±Mn, Mg and P)
Phyllic	Au	Y-V-Cu-Fe-Ti-Zr-Nb(±Al)
Phyllic	Cu	Zn-Y-Fe-Al-Si-S-Ti
Phyllic	Zn	Cu-Fe-Al-Si-S-Y
Propylitic	Au	P-Y-V-Zn
Propylitic	Cu	S-Mg-P-Ca-Rb-Sr-Pb (±K)
Propylitic	Zn	P-K-Rb-Mn-Fe (±Y)
Iron oxide-hydroxide minerals	Au	Cu-P-Y-S-As (±Cr-Al-Ti-V)
Iron oxide-hydroxide minerals	Cu	As-S-Zn-Nb-P-Rb (±Fe-Ca-Sr)
Iron oxide-hydroxide minerals	Zn	Cu-As-Nb
Silicic	Au	Cu-Rb-Zn-P-Pb-As (±Sr)
Silicic	Cu	K-Ti-V (±Rb-Fe)
Silicic	Zn	S-Y-Nb-P-Mg

APPENDIX C. SUPPLEMENT IMAGE

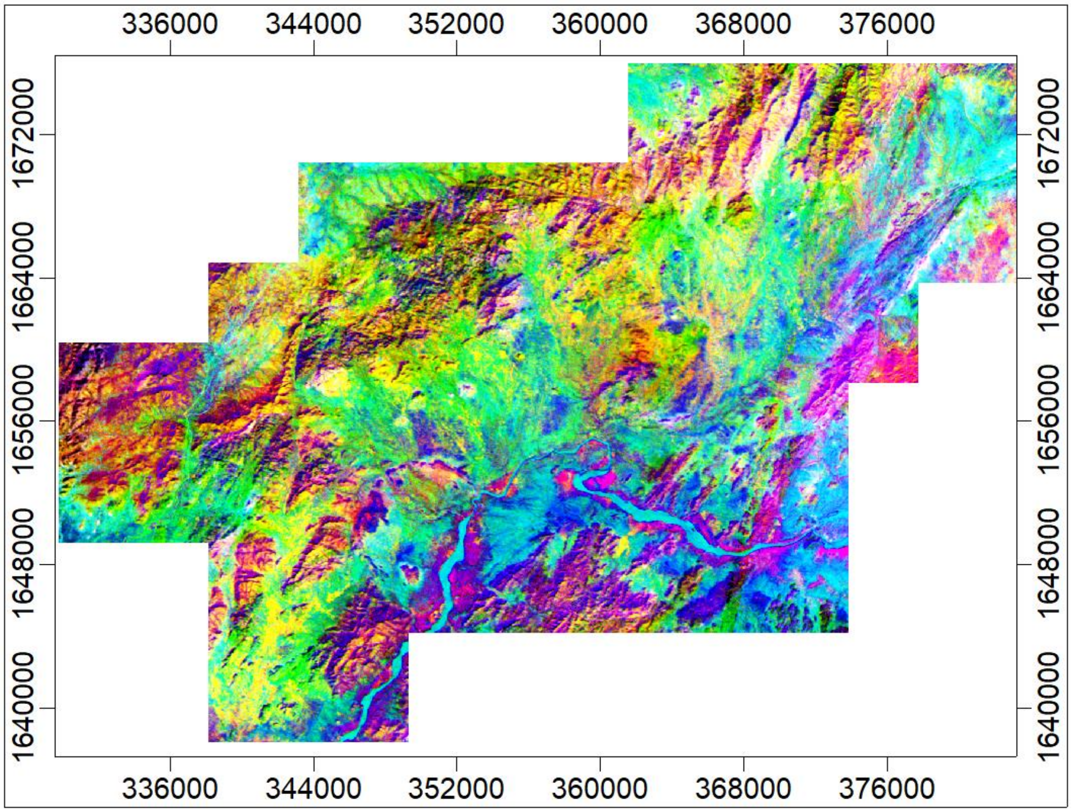

Appendix C. Fuzzified PC image in RGB: Argillic (R), Iron oxide-hydroxide minerals (G) and phyllic (B). Yellow color represents pixels containing argillic alteration and iron oxide-minerals, cyan represents phyllic alteration and iron oxide-hydroxide minerals, purple pixels are a mix of phyllic alteration and argillic, and white represents regions that contain both alterations and iron oxide-hydroxide minerals.

APPENDIX D. SUPPLEMENT BIPLOTS

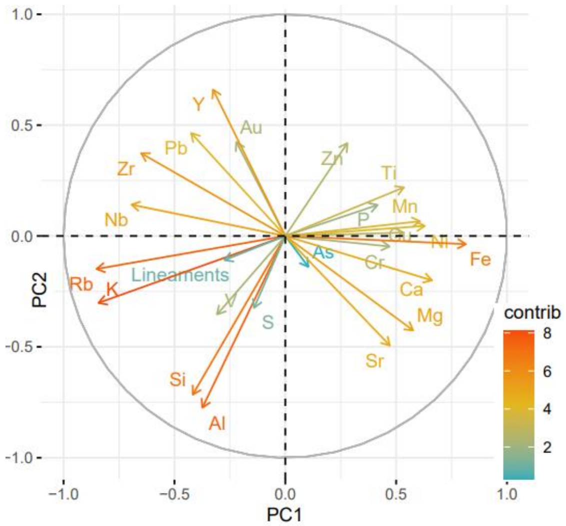

Appendix D (1). Biplot PC1-PC2

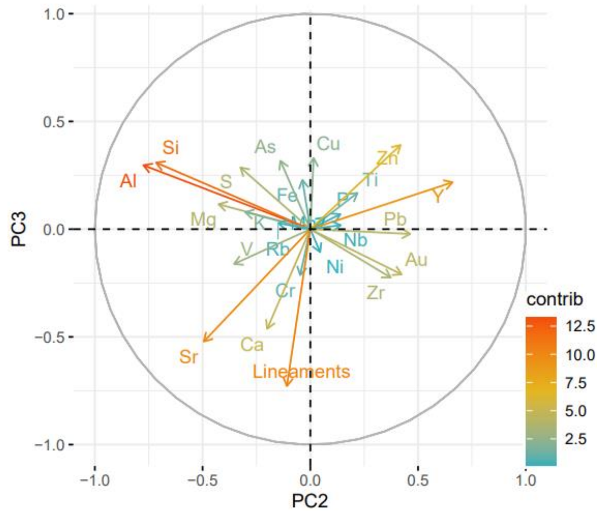

Appendix D (2). Biplot PC2-PC3

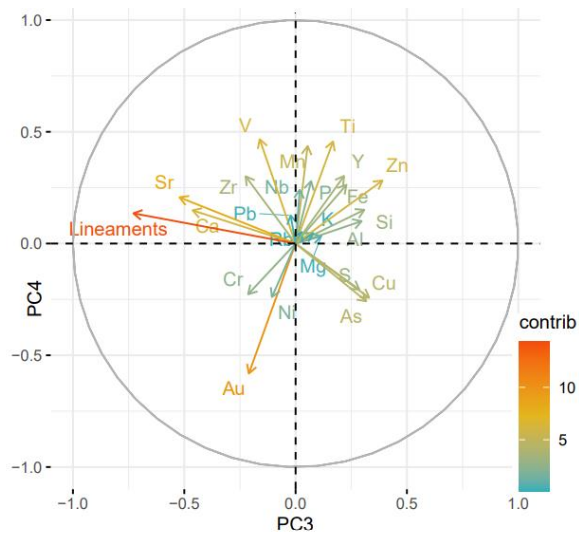

Appendix D (3). Biplot PC3-PC4

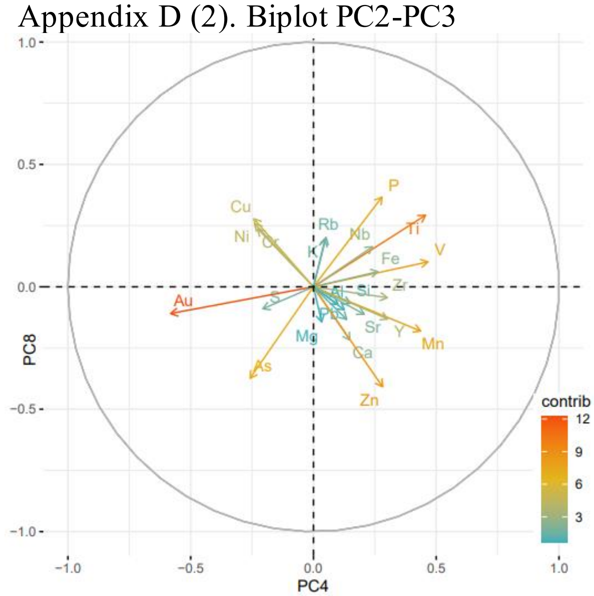

Appendix D (4). Biplot PC4-PC8